

ADA 012250

AFCRL-TR-74-0572  
PHYSICAL SCIENCES RESEARCH PAPERS, NO. 611



## An Ablation Technique for Enhancing Reentry Antenna Performance; Flight Test Results

DALLAS T. HAYES  
SHELDON B. HERSKOVITZ  
JOHN F. LENNON  
J. LEON FOIRIER

14 November 1974

Approved for public release; distribution unlimited.

D D C  
REF ID: A62914  
JUL 15 1975  
DISTRIBUTED BY  
D

MICROWAVE PHYSICS LABORATORY PROJECT 2153  
AIR FORCE CAMBRIDGE RESEARCH LABORATORIES  
HANSOM AFB, MASSACHUSETTS 01731

AIR FORCE SYSTEMS COMMAND, USAF



1427

**Qualified requestors may obtain additional copies from the Defense Documentation Center. All others should apply to the National Technical Information Service.**

Unclassified

SECURITY CLASSIFICATION OF THIS PAGE (When Data Entered)

REPORT DOCUMENTATION PAGE		READ INSTRUCTIONS BEFORE COMPLETING FORM
1. REPORT NUMBER	11. GOVT ACCESSION NO.	3. RECIPIENT'S CATALOG NUMBER
AFCRL-TR-74-0572, AFCRL-PSRP-611		
4. TITLE (and subtitle)		5. TYPE OF REPORT & PERIOD COVERED
AN ABLATION TECHNIQUE FOR ENHANCING REENTRY ANTENNA PERFORMANCE; FLIGHT TEST RESULTS		Scientific Interim
7. AUTHOR(s)		6. PERFORMING ORG. REPORT NUMBER
Dallas T. Hayes, Sheldon B. Herskovitz, John F. Lennon ■ J. Leon Poirier		PSRP 611
8. PERFORMING ORGANIZATION NAME AND ADDRESS		8. CONTRACT OR GRANT NUMBER(s)
Air Force Cambridge Research Laboratories (LZP) Hanscom AFB Massachusetts 01731		(17) (16)
11. CONTROLLING OFFICE NAME AND ADDRESS		10. PROGRAM ELEMENT, PROJECT, TASK AREA & WORK UNIT NUMBERS
Air Force Cambridge Research Laboratories (LZP) Hanscom AFB Massachusetts 01731		641001 681375 6460010
14. MONITORING AGENCY NAME & ADDRESS (if differen. from Controlling Office)		12. REPORT DATE
		14 Nov 1974
16. DISTRIBUTION STATEMENT (of this Report)		13. NUMBER OF PAGES
Approved for public release; distribution unlimited.		80
17. DISTRIBUTION STATEMENT (of the abstract entered in Block 20, if different from Report)		15. SECURITY CLASS. (of this report)
(1) Physical sciences research program,		Unclassified
18. SUPPLEMENTARY NOTES		16a. DECLASSIFICATION/DOWNGRADING SCHEDULE
19. KEY WORDS (Continue on reverse side if necessary and identify by block number)		
Reentry flight test Plasma alleviation Teflon ablation Microwave flight test measurements Electrostatic probe measurements		High-power pulse measurements
20. ABSTRACT (Continue on reverse side if necessary and identify by block number)		To develop alternative solutions to Air Force problems relating to signal transmission in the presence of ionization, AFCRL undertook an extensive investigation of techniques for modifying reentry plasmas. The program included laboratory tests and a series of reentry flight experiments. This report describes the flight test of one successful technique, Teflon ablation, a passive approach that requires no internal support systems.

**DD FORM 1473 EDITION OF 1 NOV 65 IS OBSOLETE**  
JAN 73

Unclassified

Unclassified

SECURITY CLASSIFICATION OF THIS PAGE (When Data Entered)

Unclassified

(contd.)

D D G

JUL 15 1975

תְּהִלָּה בְּשֶׁבֶת

二

D

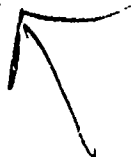
Unclassified

SECURITY CLASSIFICATION OF THIS PAGE(When Data Entered)

(Block 20 contd)

A reentry vehicle fitted with a Teflon-coated nosecap was instrumented to measure antenna impedance mismatch, interantenna coupling, signal attenuation, and charged-particle density. The probe data showed that the local boundary-layer electron density decreased by as much as a factor of 200. The Teflon coating effected a 25-dB decrease in S-band signal attenuation. High-power antenna breakdown was modified by the presence of the ablation products.

Details of the vehicle design, flight dynamics, and ablation, are presented, and the results of the Teflon-ablation technique are contrasted with those of a successful liquid-injection technique that was tested on a previous flight.



Unclassified

SECURITY CLASSIFICATION OF THIS PAGE(When Data Entered)

## Preface

The AFCRL program for enhancing reentry antenna performance owes its success to the efforts of many contributors. R. Walters of the Aerospace Instrumentation Laboratory was responsible for the mechanical features of the Teflon flight. Many of the electronic systems and signal-processing circuits were designed, tested, and installed in the payload, by R. Sukys, of Northeastern University. Teflon was applied to the nosecap by the M. I. T. Aerophysics Laboratory, directed by Professor C. W. Haldeman. The AFCRL machine shop headed by W. Mathison fabricated the mechanical hardware, diagnostic probes, and microwave antennas. S. Goldberg of Northeastern University; and J. Antonucci, D. Jacavanco, N. Karas, and D. Tropea, all of the Microwave Physics Laboratory, were of valuable assistance. The overall program was under the supervision of W. Rotman, Chief of the Hypersonic Electromagnetics Branch.

The experimental vehicle was assembled and launched from the NASA Flight Test Facility at Wallops Island, Va. P. White directed the work; D. Bruton was the NASA Project Engineer.

The generous cooperation of all that participated in this endeavor is gratefully acknowledged.

## **Contents**

1. INTRODUCTION	9
2. DESCRIPTION OF THE VEHICLE AND THE EXPERIMENT	10
3. VEHICLE FLIGHT PERFORMANCE	14
4. THE ABLATION PROCESS	19
4.1 The Ablative Material	19
4.2 Heat Transfer and Ablation	20
4.3 Ablated Teflon-Air Interaction	23
4.4 Comparative Thermochemistries of Teflon and Freon 114B2	27
5. ANTENNA MEASUREMENTS	28
5.1 S-Band Low-Power Experiment	30
5.2 High-Power Test System	38
5.3 Secondary S-Band Test/TM System	45
6. ELECTROSTATIC PROBE DATA ANALYSIS	47
6.1 General Description of Probes	47
6.2 Theory	48
6.3 Rationale of Probe Location	53
6.4 Probe Results	54
7. COMPARISON OF THE ABLATIVE AND LIQUID-INJECTION FLIGHTS	64
7.1 Additive Comparisons	64
7.2 Probe Results	66
7.3 Antenna Results	68
8. DISCUSSION OF EXPERIMENTAL RESULTS	70

## Contents

9. CONCLUSIONS	71
REFERENCES	73
APPENDIX A: Ablative Gauges	75
SYMBOLS	79

## Illustrations

1. General Features of a Typical Trailblazer II Trajectory	11
2. Location of Probes and Antennas on Nose Cone (sketch)	12
3. Ablation Flight Trajectory Parameters	15
4. Freestream Velocity, Mach Number, and Unit Reynolds Number	17
5. Stagnation Enthalpy, Pressure, and Heat Transfer Rate	17
6. Transition to Turbulence	18
7. Frequency of Cyclic Variations in Test Data	19
8. Surface Heat Transfer Rates at Selected Altitudes	21
9. Nosecap Recession at Selected Altitudes	22
10. Estimated Nosecap Ablation	23
11. Air Mass Flow in Nosecap Boundary Layer	24
12. Teflon/Air Mole Fractions	25
13. Low-Power Test System (simplified block diagram)	30
14. Sketch of Vehicle Surface Cut Away to Show Low-Power Test System	31
15. Nose Cone Spin Rate	32
16. Low-Power Reflection Coefficient	32
17. Variation in Low-Power Reflection Coefficient During One Spin Cycle	34-35
18. Interantenna Coupling Loss	36
19. Variation in Low-Power Interantenna Coupling Loss During One Spin Cycle	37
20. Total Signal Attenuation (Low Power)	39
21. High-Power Test System (simplified block diagram)	40
22. Typical High-Power Incident and Reflected Pulses	40
23. High-Power Reflection Coefficient	42
24. High-Power Reflection Coefficient at Selected Altitudes	42

## Illustrations

25. Power Required for Antenna Breakdown (laboratory experiment)	43
26. Computed Boundary-Layer Pressure at the Shoulder	43
27. Comparison of High- and Low-Power Reflection Coefficients	44
28. Telemetry/Secondary Test System (simplified block diagram)	45
29. Power Reflection Coefficient of TM/TX Antenna	46
30. Total Signal Attenuation Measured by Main Base MGT and ADAS	47
31. Cross-Sectional View of ES Probe Assembly	48
32. Unmodified Positive-Ion Density Measured at $S/R_N = 1.77$ on Fourth Flight	55
33. Charged-Particle Densities Measured at $S/R_N = 1.77$ on Fifth Flight	55
34. Charged-Particle Densities Measured at $S/R_N = 2.40$ on Fifth Flight	58
35. Charged-Particle Densities Measured at $S/R_N = 4.44$ on Fifth Flight	59
36. Electron Density Measured at $S/R_N = 2.40$ on Fifth Flight	61
37. Comparison of Predicted and Measured Transition to Turbulence	64
38. Relative Alleviant Concentrations	65
39. Typical Charged-Particle Concentrations Measured During Fourth Flight (Freon-injection)	66
40. Effect of Alleviants on Electron Density	68
41. Effect of Alleviants on Total Signal Attenuation	69
A1. Electrical Subassembly of Ablation Gauge (schematic)	76
A2. Assembly of Ablation Gauge (sketch)	77
A3. Components of Ablation Gauge	78

## Tables

1. Antenna and Probe Locations and Identifications	13
2. Vehicle and Flight Parameters for the Teflon Ablation Flight	14
3. Typical Radar Data From the Teflon Ablation Flight	16
4. Mole Fraction of Species in Equilibrium at 1 Atm	26
5. Comparison of Calculated Negative-Ion Current and Measured Total Probe Current	52
6. Significant Reentry Events Determined From Probe Data	63

## An Ablation Technique for Enhancing Reentry Antenna Performance; Flight Test Results

### 1. INTRODUCTION

The operation of microwave antenna systems during reentry and techniques for controlling shock-induced ionization have been investigated by the AFCRL Microwave Physics Laboratory. Theoretical predictions and results obtained in the laboratory were combined with a flight test program in which five Trailblazer<sup>II</sup> rockets were launched from Wallops Island, Va.<sup>1-3</sup> For all five tests the trajectory and flight parameters, as well as the physical characteristics of the nose cone, were identical. There was extensive diagnostic instrumentation on each flight; and a number of microwave and probe measurements on successive flights were similar. The combined results yielded data for a wide range of correlations.

The flight tests were organized in two phases. In the first, consisting of three flights, the effect of reentry ionization on signal transmission was determined, and probes for measuring the ionization directly were tested. On the last

(Received for publication 12 November 1974)

1. Poirier, J. Leon, Rotman, Walter, Hayes, Dallas T., and Lennon, John F. (1969) Effects of the Reentry Plasma Sheath on Microwave Antenna Performance: Trailblazer II Rocket Results of 18 June 1967, AFCRL-69-0354.
2. Hayes, Dallas T., and Rotman, Walter (1973) Microwave and electrostatic probe measurements on a blunt reentry vehicle, AIAAJ 11:675-682.
3. Hayes, Dallas T., Herskovitz, Sheldon R., Lennon, John F., and Poirier, J. Leon (1972) Preliminary Report on the Trailblazer II Chemical Alleviation Flight of 28 July 1972, AFCRL-72-0840.

two flights, chemical alleviation techniques were evaluated. An additional feature on the final flight was an experiment to acquire data on the effectiveness of chemical additives in retarding antenna voltage breakdown under reentry conditions.

On the fifth flight, the vehicle nosecap was covered with a layer of Teflon. This material ablated during reentry, releasing electrophilic decomposition products. On the fourth flight, electrophilic liquid Freon 114B2 had been carried on board the vehicle and injected over the test antenna. Since Teflon and Freon 114B2 have similar decomposition histories, a number of comparisons between the two techniques are thus possible.

This report presents experimental data from the fifth flight, preliminary analyses, comparisons with earlier flights, and some indications of significant trends and results. A reference list of symbols follows Appendix A.

## 2. DESCRIPTION OF THE VEHICLE AND THE EXPERIMENT

The reentry nose cone was launched on a Trailblazer II vehicle, a four-stage solid-propellant rocket. The first two stages lifted the vehicle to an altitude of about 200 miles. The last two stages propelled the reentry nose cone back toward the atmosphere along an almost vertical trajectory.

During ascent the vehicle was fin-stabilized. Shortly after launch, the canted second-stage fins induced spinning, and as the vehicle left the atmosphere its spin rate was high enough to ensure spin-stabilization throughout the remainder of the flight.

The last two stages were enclosed in a structural shell (velocity package, shown in Figure 1) and faced rearward during launch. At about 250 kft, the velocity package separated from the spent second-stage motor and coasted to apogee. As the velocity package began its descent, the third-stage motor fired, propelling the reentry nose cone out of the open end of the velocity package. The 15-in. fourth-stage spherical motor provided the final thrust necessary to boost the velocity to about 17,000 fps by the time the nose cone began reentry.

The nose cone was a 9° hemisphere-cone fabricated entirely of aluminum. Its total length was 26.47 in., and its base diameter was 19.17 in. Before the Teflon covering was applied, the nosecap radius was 6.333 in. The instrumented nose cone weighed about 72 lb, including the spent fourth-stage motor.

The nose cap was covered with a hemispheric Teflon shell whose thickness ranged from 0.5 in. at the stagnation point to about 0.1 in. where it ended, just forward of the hemisphere-cone junction. The ablation products of this Teflon layer were swept back over the body and modified the chemical properties of the flow. The principal effect was a reduction in the free electron concentration.

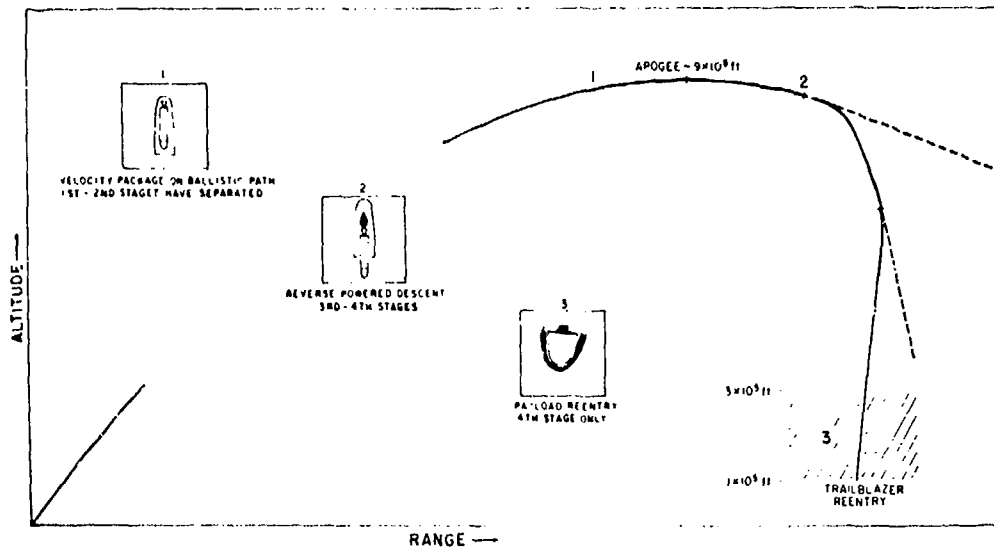


Figure 1. General Features of a Typical Trailblazer II Trajectory

This experiment was designed to obtain specific measurements of the plasma sheath and data on the behavior of microwave radiating and receiving systems in the presence of ablating Teflon. The payload consisted of five functional systems: the telemetry and secondary test system (2220.5 MHz); the low-power test transmitting and receiving system (2290.5 MHz); the high-power test transmitting system (2255 MHz, 1 kW peak power); a set of eight electrostatic probes; and five ablation gauges.

The S-band telemetry system (TM/TX) transmitted flight measurements to the ground. It also served as a secondary test source for antenna impedance and signal-attenuation measurements.

The low-power test system was used to observe effects of the plasma sheath and chemical additive on interantenna coupling, antenna impedance mismatch, antenna pattern distortion, and signal attenuation.

The high-power test system was used to observe the effect of the chemical additive on the antenna voltage breakdown. It was also used to measure impedance mismatch and signal attenuation.

The eight electrostatic probes determined electron and ion densities near the surface of the vehicle. This dual measurement was necessary to assess the

effectiveness of the ablating Teflon. The bias potential of some of the probes was periodically switched during the flight to obtain results at several distances from the surface.

The five ablation gauges were located to measure the rate of ablation and its uniformity around the nosecap.

The various antennas, probes, and gauges are shown in Figure 2 and listed in Table 1. The relative placement of the probes and antennas was based on the behavior of the plasma sheath predicted from previous flight data and the measurement goals of this flight. For example, the low-power and high-power test transmitting antennas were located at the same station but opposite one another

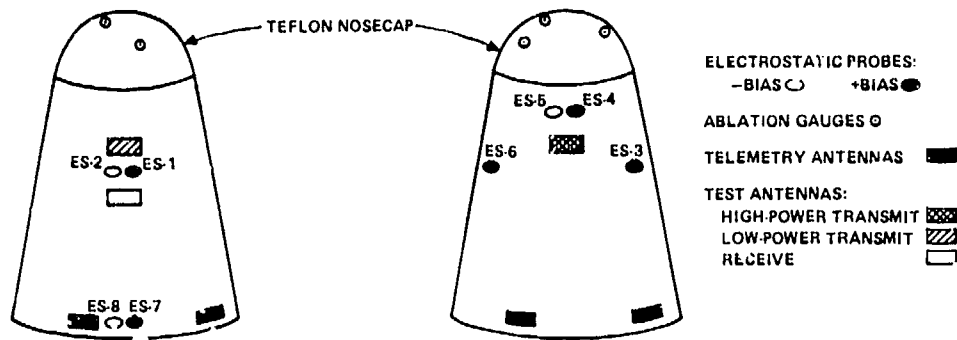


Figure 3. Location of Probes and Antennas on Nose Cone (sketch)

on the nose cone so that they were alternately exposed to the same plasma conditions as the vehicle rotated and a direct comparison could be made between the two. These antennas were located at a station where the local ionization was high enough to ensure a significant effect. In contrast, the telemetry antennas were placed as far back on the cone as possible so as to minimize the influence of the ionization on their operation. The electrostatic probes were located near the antennas so that the charged-particle densities could be determined at those positions. Some of the probes were located at the same location as those on the Freon injection flight so that direct comparisons could be made between the results of the two experiments.

Table 1. Antenna and Probe Locations and Identifications

Device		Bias Voltage	Station (in.)	S/R <sub>N</sub>	$\phi$ Clockwise
Type	Symbol				
Flushmounted Electrostatic Probes	ES-1	Positive 15, 30	11.51	2.40	355.5°
	ES-2	Negative 15, 30			4.5°
	ES-3	Positive 15			111.0°
	ES-4	Positive 15	7.58	1.77	175.5°
	ES-5	Negative 15			184.5°
	ES-6	Positive 15	11.51	2.40	249.0°
	ES-7	Positive 15	24.27	4.44	355.5°
	ES-8	Negative 15			4.5°
Low-Power Test Antenna, Transmitting	TX		9.57	2.09	0°
Test Antenna Receiving	RX		13.46	2.71	0°
High-Power Test Antenna, Transmitting	TXH		9.57	2.09	180.0°
Telemetry Antennas	TM-1		24.27	4.44	105.5°
	TM-2				195.5°
	TM-3				285.5°
Secondary Test/ Telemetry Antenna	TM/TX				15.5°
Ablation Gauges	AB-1			0.18	15.0°
	AB-2			0.48	105.0°
	AB-3			0.18	195.0°
	AB-4			0.79	225.0°
	AB-5			0.79	345.0°

 $\phi$  Measured from test antenna location

### 3. VEHICLE FLIGHT PERFORMANCE

The vehicle parameters and the resulting trajectory dynamics are briefly summarized in Table 2. The complete payload trajectory is shown in Figure 3(a) with significant events during the flight indicated. To place the experimental results in proper context with regard to atmospheric conditions, the velocity and altitude time histories are shown in Figure 3(b). Because of the thermal protection given by the ablating heat shield, the useful trajectory was extended to rather low altitudes compared with those of the earlier flights, where protection depended on a heat sink method. The peak velocity of 17,000 fps represents the median of the series. It is somewhat higher than that attained in the injection flight, which

Table 2. Vehicle and Flight Parameters  
for the Teflon Ablation Flight

Launch	6 Dec 1973 (2259Z)
Payload weight	82.5 lb
Ballistic coefficient $\beta$	102.8 lb/ft <sup>2</sup>
Angle of attack	12.8°
Spin rate	11.4 rps
Transverse moment of inertia $I_T$	1.21 slug ft <sup>2</sup>
Axial moment of inertia $I_A$	0.56 slug ft <sup>2</sup>
Center of gravity (distance from base)	16.4 in.
Telemetry	S band (at base of cone)
Apogee	997,743 ft
Peak velocity	17,000 fps (at 211 kft)
Reentry flight azimuth	350.6°
Time from launch to reentry (300 kft)	407.9 sec
Reentry flight path angle $\gamma$	-79.2°
Third-stage burn time	39.2 sec
Fourth-stage burn time	4.9 sec
Onset of plasma effects (shoulder region ES probes)	270 kft
Ablative material	Teflon ( $C_2F_4$ )
Coating thickness (at center of nose)	0.5 in.

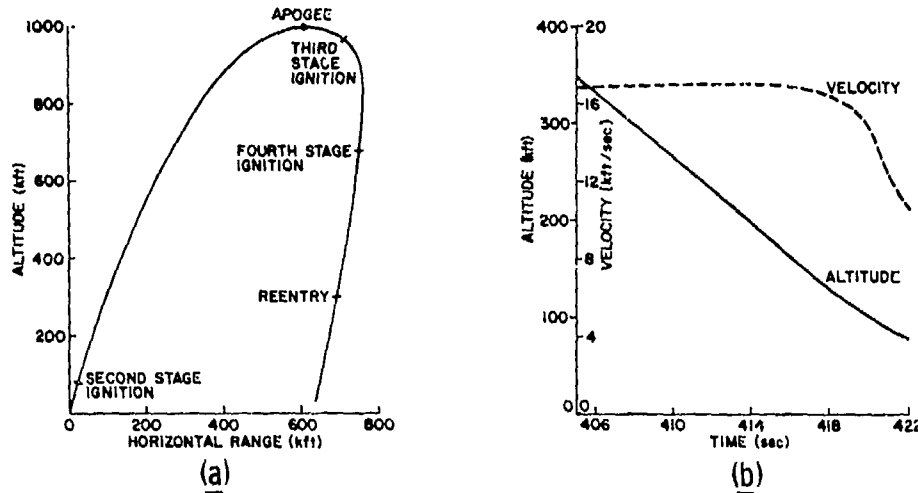


Figure 3. Trailblazer Teflon-Ablation Flight Data Based on AN/FPQ-6 Radar Results [(a) trajectory; (b) time history of altitude and velocity]

reached 16,240 fps, and so the plasma conditions should have been slightly more severe in the present case. As a whole, the performance was typical of the series. The low value of the ballistic coefficient  $\beta \approx 100 \text{ lb/ft}^2$  and the reentry flight path  $\gamma \approx -79^\circ$  were also characteristic.

Table 3 lists some of the processed radar data for the payload in its final freefall mode. The 500-kft altitude represents a point just after burnout of the fourth-stage motor; the 150- and 100-kft altitudes are representative of the reentry phase.

Figure 4 shows the freestream velocity, Mach number, and unit Reynolds number as a function of altitude. The Mach number decreases with altitude but remains hypersonic until below 80 kft. The freestream Reynolds number increases continuously from  $Re_\infty \approx 10^3$  at 280 kft to  $Re_\infty \approx 5 \times 10^6$  at 65 kft, but below 100 kft the growth begins to decline as the vehicle decelerates. Figure 5 shows the resulting stagnation pressure also increasing, reaching  $p_{ST} \approx 6.4 \text{ atm}$  at 65 kft. The stagnation enthalpy remains essentially constant at  $h_{ST} \approx 3200 \text{ cal/gm}$  until after the peak deceleration has occurred near 120 kft. The peak cold-wall laminar heating rate at the stagnation point  $q_{ST} \approx 450 \text{ Btu/ft}^2 \cdot \text{sec}$  is seen to occur in that same maximum heating regime near 100 kft. For turbulent conditions, the peak heating occurs at the point where the flow becomes sonic near the vehicle surface. That profile is not shown since for the actual flight the onset of turbulence at that location did not occur until the vehicle was below 75 kft.

Table 3. Typical Radar Data From the Teflon Ablation Flight

Property	Altitude (kft)		
	500	150	100
Slant range (ft)	895,104	688,277	669,582
Azimuth (deg)	155.2	153.7	153.5
Elevation (deg)	32.9	11.6	7.7
Horizontal range (ft)	720,625	657,226	648,364
Velocity (fps)	16,530	16,772	14,822
Latitude (deg)	36.03	36.21	36.2
Longitude (deg)	-74.47	-74.51	-74.5
North-South range (ft)	-654,331	-589,558	-580,418
Look range (ft)	885,228	676,697	657,859
East-West velocity (fps)	-549.0	-494.0	-417.0
North-South velocity (fps)	3,093	3,094	2,760
Flight elevation (deg)	-79.05	-79.23	-79.15
Visual azimuth (deg)	155.22	153.76	153.53
Look azimuth (deg)	155.27	153.78	153.54
Look elevation (deg)	33.38	11.86	7.87
East-West range (ft)	301,962	290,499	288,985
Altitude velocity (fps)	-16,229	-16,477	-14,557
Flight azimuth (deg)	349.93	350.92	351.41

The transition from laminar to turbulent conditions in the boundary layer is a complex process difficult to characterize. Ablation adds to the uncertainty, and the fact that the transition distance can be finite presents a further complication. The effect of roughness on transition can become significant when mean height  $k$  is comparable to the momentum thickness  $\theta$ . A number of curve fits for the transition have been devised from experimental results.<sup>4-6</sup> The transition criteria are generally related to the local Reynolds number based on momentum thickness  $Re_\theta$ .

Given the range of possible formulations, a simple criterion was selected for transition:  $Re_\theta \approx 240$ . The transition was assumed to be instantaneous. For the

4. Strategic Reentry Technology Program (STREET A) (1970) Task 7.5: Nose Tip Ablation Phenomena, Final Rpt, Vol. II, SAMSO-TR-70-247.
5. van Driest, E. R., Blumer, C. B., and Wells, C. S. (1967) Boundary-layer transition on blunt bodies—effect of roughness, AIAAJ 5:1913-1915.
6. Nosetip Design Analysis and Test Program (NDAT) (1971) Final Rpt, Vol. I, Part 1, SAMSO-TR-71-11.

Figure 4. Freestream Velocity, Mach Number, and Unit Reynolds Number

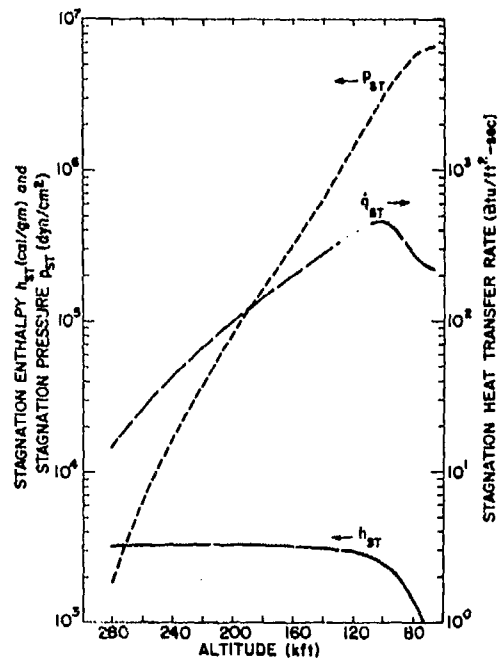
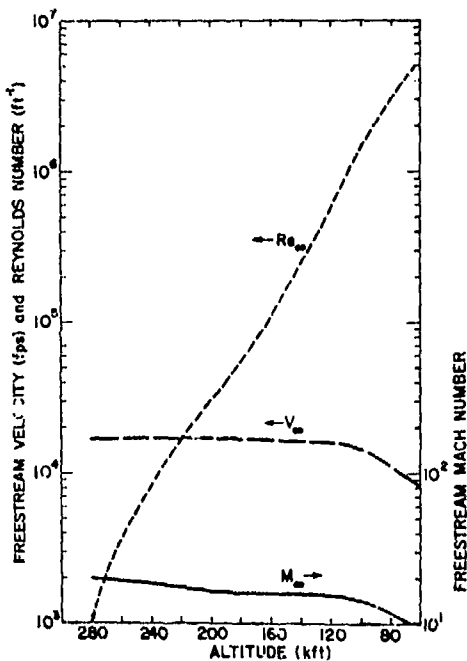


Figure 5. Stagnation Entropy, Pressure, and Heat Transfer Rate

fifth flight, variation of the Reynolds number with altitude was computed according to Detra and Hidalgo's approach<sup>7</sup> and plotted in Figure 6, which shows that the turbulence advances rapidly from the rear of the vehicle but slows down drastically in the region of the ablating nosecap. Beginning at about 120 kft, it rushes from rear to shoulder during an altitude change of less than 2 kft. It then slows down, reaching the sonic point only below 75 kft.

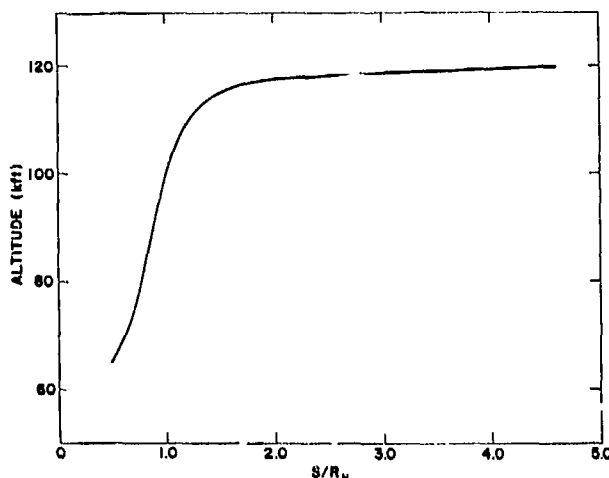
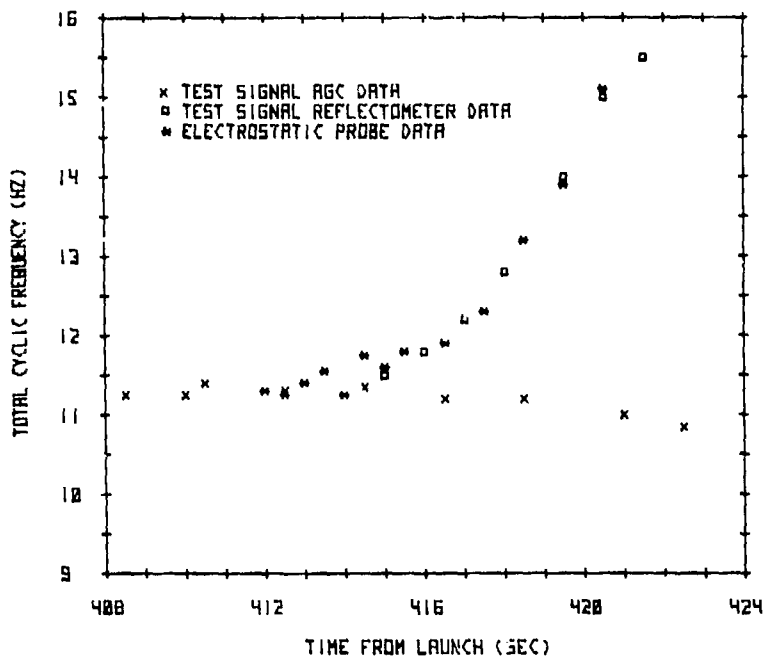


Figure 6. Transition to Turbulence ( $Re_\theta \approx 240$ )

Analysis of the experiment is complicated because (1) the vehicle was spin-stabilized; and (2) at altitudes below 200 kft, aerodynamic forces cause additional precessional effects. Figure 7 shows the total cyclic frequency in the test data, from which the spin and precession can be derived. Down to 200 kft, the basic spin rate was 11.4 rps; below the 200-kft level, at approximately 414 sec from launch, precession increased the total cyclic frequency. The eventual spin decrease at the lower altitudes is indicated by the Xs in Figure 7. Determination of these quantities involves analysis of various antenna and probe data (see Sec. 5).

Preliminary evaluation of the data relating to the fifth flight indicates that the vehicle reentered the atmosphere at an estimated  $12.5^\circ$  angle of attack, as opposed to the  $16.5^\circ$  angle on the fourth flight. The smaller angle of attack should tend to keep the windward values of electron density somewhat closer to the zero angle levels. This difference in angle of attack should compensate for the slower reentry velocity on the fourth flight. Thus, in the absence of any modification process, the windward cases for the two tests should be similar.

7. Detra, R. W., and Hidalgo, H. (1961) Generalized heat transfer formulas and graphs for nose cone reentry into atmosphere, ARSJ 31:318-321.



per hour at 500°K; about 0.004% at 650°K. Under the reentry conditions of this experiment, the amount of material sublimed is calculated according to thermodynamic considerations, using an effective heat of ablation for the Teflon coupled with the enthalpy delivered by varying flow conditions. The sublimed Teflon products undergo further decomposition in the hot air surrounding the reentry vehicle. Several of these decomposition products—for example,  $\text{CF}_4$ ,  $\text{CF}_2$ , and F—display electrophilic properties of varying degrees.

#### 4.2 Heat Transfer and Ablation

The descent of the vehicle through the atmosphere causes an interaction between the body and the air flowing around it. Drag forces produce vehicle deceleration, and the formation of a surrounding high-temperature shock layer tends to heat the nose cone.

On previous flights the aluminum nose had acted as a heat sink. The surface temperatures had remained relatively unchanged until after the period of maximum deceleration and heating, at around 100 kft, when the data became uncertain.

On the present flight, the low thermal conductivity of Teflon allowed little heat transfer through the nose cap layer. The aerodynamic heat input caused sublimation of the Teflon surface, and the ablated material was a further block to heat transfer from the boundary layer. This heat shield mechanism gave more effective protection than the heat sink method used on previous flights, and so this nose cone survived to lower altitudes and yielded more data.

The heat transfer rate at stations along the hemispheric cap depends on local conditions in the boundary layer, which change greatly along the trajectory. Even at a given altitude, there is considerable variation with position since the flow is expanding and cooling as it moves away from the nose stagnation region. In addition, turbulence in the boundary layer may occur at some point along the surface, resulting in a thicker layer with greater heat transfer. There is thus a dependence on altitude, velocity, and vehicle configuration.

Extended exposure to high rates of heating can result in considerable erosion of the ablator, and nonuniformity of the heating can cause nosetip recession and an altered vehicle profile. In the present case, however, the conditions were not that severe, and it was assumed that the vehicle shape remained unchanged over the entire flight.

Detra and Hidalgo's<sup>7</sup> laminar and turbulent heat transfer relations were used to calculate two heating histories along the trajectory. The transition from laminar to turbulent flow was taken to be instantaneous, and its occurrence at a particular location was determined from Figure 6. The laminar heat transfer rate was determined from the expression:

$$\dot{q} = \left[ 865 (V/10^4)^{3.15} R_N^{-1/2} \left( \rho_\infty / \rho_{SL} \right)^{1/2} \left( \frac{h_e - h_w}{h_e - h_{cw}} \right) \right] \Psi ,$$

which assumes a Newtonian velocity gradient at the stagnation point, equilibrium flow, Sutherland temperature-dependence for viscosity, Lewis number of 1.4, and Prandtl number of 0.71. The corresponding expression for turbulent conditions,

$$\dot{q} \approx 1.346 \times 10^4 \left( \rho_\infty / \rho_{SL} \right)^{0.6} (V/10^4)^{3.18} S^{-1/2} \Phi ,$$

assumes a representative specific heat ratio  $\gamma = 1.2$  for the isentropic flow around the body. The equations contain factors ( $\Psi, \Phi$ ) that take the body geometry and pressure gradient into account.

For the fifth flight these relations were used to compile a composite history of the heat transfer around the nose cap as a function of altitude. This is shown in Figure 8. Above 120 kft the flow was completely laminar. The 100-kft and 75-kft curves indicate the advance of turbulence toward the nose. Note that there was no attempt to include transitional heating in the results.

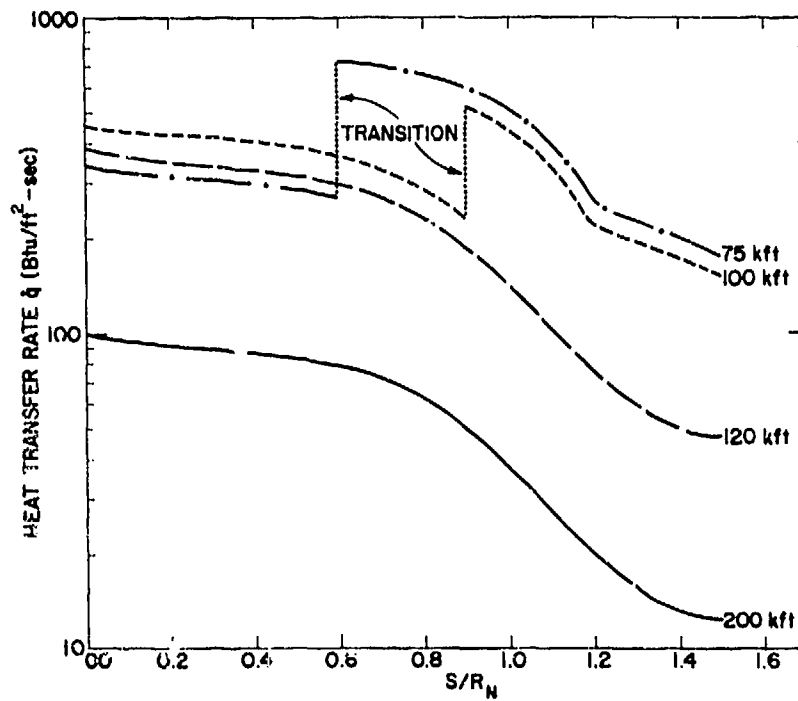


Figure 8. Surface Heat Transfer Rates at Selected Altitudes

To examine the effect of heating on the ablative coating during reentry, a time of flight  $\Delta t$  was defined as the time it took the vehicle to descend from one representative altitude to the next. Heat transfer  $\Delta q$  during that interval was then determined from  $\Delta q = \dot{q} \times \Delta t$ .

The basic heat transfer equations require some modification for an ablative surface since the mass transfer acts to shield the surface. The amount of material leaving the surface is determined from an effective heat of ablation  $h_{\text{eff}}^{\circ}$ . For Teflon this has the form:<sup>8</sup>

$$h_{\text{eff}}^{\circ} = 950 + 0.49 (h_e - h_w), \text{ laminar.}$$

and

$$h_{\text{eff}}^{\circ} = 950 + 0.16 (h_e - h_w), \text{ turbulent,}$$

where  $h_e$  and  $h_w$  are respectively the enthalpy at the outer edge of the boundary layer and at the hot wall. The recession history for the nosecap as a function of altitude (Figure 9) is then obtained by summing the change in thickness of the abla-

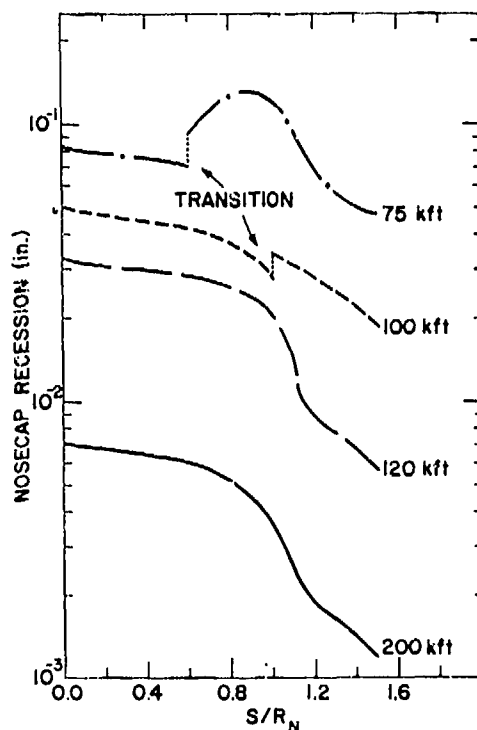


Figure 9. Nosecap Recession at Selected Altitudes

8. Martin, J. J. (1966) Atmospheric Reentry: An Introduction to its Science and Engineering, Prentice-Hall, p. 114.

tive coating.

$$\Delta d = (\rho_{C_2F_4})^{-1} \left( \Delta q / h_{\text{eff}}^{\circ} \right).$$

As can be seen, the ablation is a relatively small effect until the vehicle has reached the lower altitudes.

The total alteration in the original Teflon covering at the end of the useful trajectory is depicted in Figure 10. The estimated ablation for the actual flight conditions did not exceed design limits except at the shoulder, where the shell was relatively thin to allow fairing into the metal afterbody.

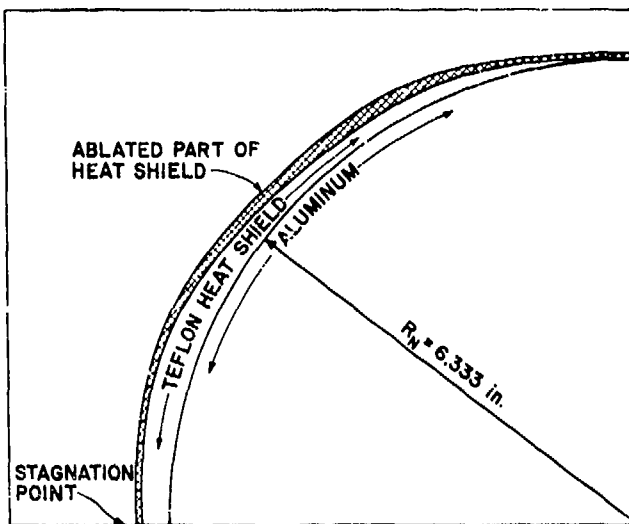


Figure 10. Estimated Nosecap Ablation

#### 4.3 Ablated Teflon-Air Interaction

A primary topic of interest in this flight test was whether the free-electron concentration in the boundary layer would be reduced by cooling and electrophilic action of the ablated Teflon. As a first step, the relative concentrations of Teflon and air were determined as a function of altitude.

The air flow was estimated by defining a capture radius equivalent to the body nose radius and assuming that the freestream air mass corresponding to that area had been swallowed into the boundary layer at the shoulder. The resulting air flow is graphed in Figure 11.

To estimate the Teflon concentration, the surface area of the nose cone was divided into spherical zones associated with the appropriate diagnostic stations. The mass of Teflon ablated from each zone was calculated as a function of altitude.

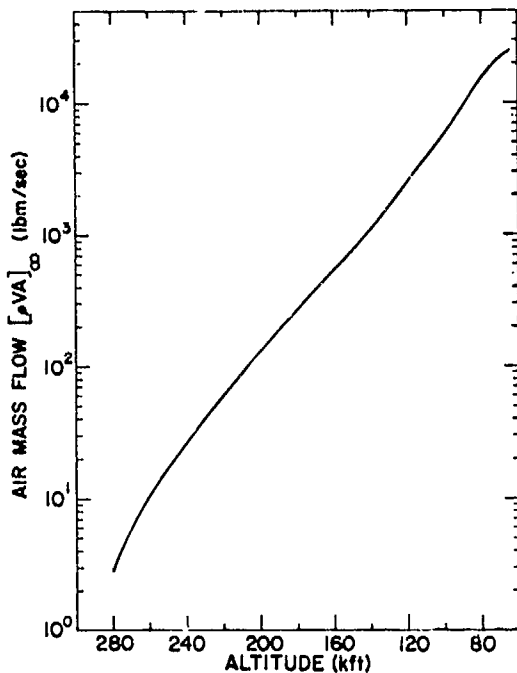
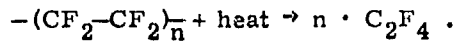


Figure 11. Air Mass Flow in Nosecap Boundary Layer

These masses were then summed over the entire nose cone and the aggregate was used to establish the ratio of Teflon to air in the mixture carried downstream over the test antennas. Plotted in Figure 12, it shows that the mole fraction was generally less than 10%, and even less than 1% for a considerable altitude range.

This rather simplistic approach to characterizing the Teflon-air mixture in the boundary layer gives no details of the structure of the combined flow. To understand the electrophilic action that occurs as the mixture is swept over the vehicle afterbody requires a more precise discussion of high-temperature Teflon-air chemical kinetics.

At temperatures in excess of 1000°K, the Teflon polymer undergoes rapid decomposition into the monomer tetrafluoroethylene:



The gaseous monomer enters the high-temperature flow field and reacts with the ambient air species. The major neutral equilibrium species in air at high-altitude flow-field temperatures are N<sub>2</sub>, N, and O. The monomer may thus be fractured by collisions with the nitrogen species:



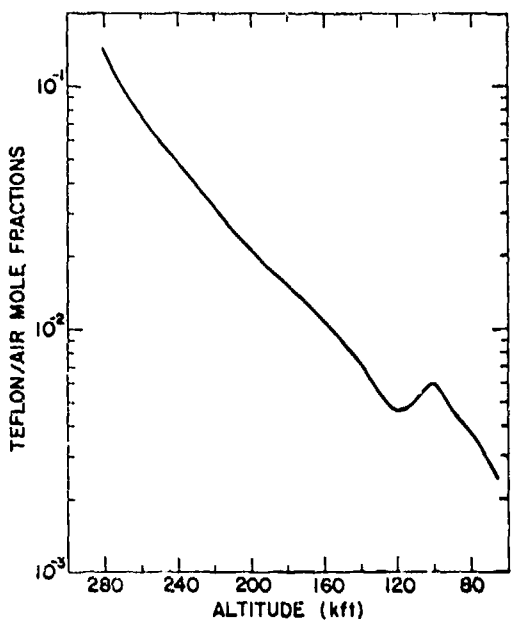
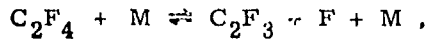
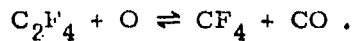


Figure 12. Teflon Air Mole Fractions  
From 60 to 280 kft

where M may be either  $N_2$  or N. This reaction, resulting in the cleavage of a C-C bond, is energetically favored over the competing mechanism:

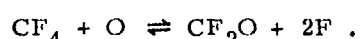
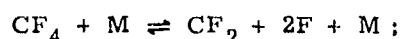


in which the more stable C-F bond ( $108 \text{ kcal mole}^{-1}$  as compared with  $88 \text{ kcal mole}^{-1}$  for the C-C bond) must be broken. The monomer may also be oxidized by collision with atomic oxygen:



Each of these reactions is reversible, and proceeds to varying degrees of completion.

The second-generation Teflon products  $CF_2$  and  $CF_4$  can further react with air species:



The species abundances actually appearing in the flow field and passing over the test antenna depend on several factors, including the relative concentrations of ablation products and air, the thermal history, and the incubation time in the flow field.

Figure 12 shows the estimated Teflon-to-air mole fractions during this experiment. When these are converted into mass ratios, a concentration in excess of 50% by weight is found at 280 kft. This ratio decreases to about 5% at 160 kft, and continues to diminish until 120 kft.

Near the ablating surface, ambient temperatures are substantially lower than within the flow field. Failure of the breakwire ablation gauge (Appendix A) suggests that the temperatures in the Teflon vapor sublayer above the ablating surface may be less than the melting point of aluminum, 933°K. Within the flow field, temperatures of 5000°K and greater may be experienced, depending on location. The effect of this concentration and temperature variation is illustrated in thermodynamic equilibrium studies of the Teflon/air system<sup>9</sup> (see Table 4).

Table 4. Mole Fraction of Species in Equilibrium at 1 Atm

Species	50% (by wt) Teflon/air		5% (by wt) Teflon/air	
	1000°K	5000°K	1000°K	5000°K
N <sub>2</sub>	0.6	0.3	0.75	0.45
CF <sub>4</sub>	0.15		0.01	
CF <sub>2</sub> O	0.08		0.01	
CO <sub>2</sub>	0.05		0.01	
CO	0.11	0.16		0.02
F		0.46		0.05
CN		0.04		
O <sub>2</sub>			0.02	
O				0.03
N				0.18

The species described in Table 4 are the principal ones found in an equilibrium mixture at 1 atm pressure. During reentry, however, particularly at the higher altitudes, incubation times in the flow and ambient particle densities may preclude chemical equilibrium.

A simple estimate can be made of the time a typical Teflon ablation product spends in the flow before passing over the test antenna. In the altitude range of

9. DeBolt, H. E., and Port, W. (1963) Thermochemical Equilibrium Studies of Ablative Heat Shield Materials, (Task 3.2, REST Project), RAD-TM-63-27, Tech Memo for AFBSD by AVCO, 7 June 1963.

280 to 110 kft, the median position of ablated mass is at an  $S/R_N$  of 0.74. This corresponds to a path of about 6.8 in. to the antenna location at an  $S/R_N$  of 1.81. An average velocity is assigned to the molecules by assuming a linear velocity profile from the surface to the edge of the boundary layer.<sup>10</sup> The resulting average transit time will be about 80  $\mu$ sec.

The number of collisions experienced by a typical ablated molecule during that time varies with molecular velocity (temperature) and contiguous air-particle density, but can be estimated from kinetic theory. In the average transit at 280 kft and a temperature of 1000°K, a Teflon-like molecule undergoes approximately 250 collisions; at 5000°K, perhaps 600 collisions. At 240 kft, at 1000°K and 5000°K, the molecular collisions number about 1000 and 2200, respectively. Of these, only collisions that have sufficient energy will produce a reaction. The degree to which any competing reaction proceeds must be evaluated from the associated rate constants. Because of the interdependence of these processes, the varying degrees of chemical equilibrium, and the changing relative composition, a computer program is required to predict the actual course of the ablation chemistry.

#### 4.4 Comparative Thermochemistries of Teflon and Freon 114B2

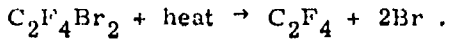
In the fourth of the Trailblazer II experiments, Freon 114B2 was injected into the flow surrounding the vehicle, and the high-vapor-pressure Freon performed well as an electrophilic agent. The Freon-air interactions are being studied by means of programs initially developed by Pergament and Kau<sup>11</sup> and subsequently refined by Hayes and Lennon.<sup>12</sup>

In the fifth flight, the solid plastic Teflon TFE was carried as an ablating electrophilic generator. Although differing markedly from Freon in physical properties and mode of delivery into the flow, it displays a similar electrophilic chemistry.

Freon 114B2 is a totally substituted ethane derivative, dibromotetrafluoroethane ( $CBrF_2-CBrF_2$ ). The compound is stable to about 900°K, at which

10. Lennon, John F. (1973) Trailblazer II Rocket Tests on the Reentry Plasma Sheath: Vehicle Performance and Plasma Prediction (Flights No. 1-3), AFCRL-TR-73-0317.
11. Pergament, H. S., and Kau, C. (1974) A Computer Code to Predict the Effects of Electrophilic Liquid Injection on Reentry Plasma Sheath Properties, AFCRL-TR-74-004, Contract No. F19628-93C-0045, Aerochem. Res. Lab., Inc.
12. Hayes, Dallas T., and Lennon, John F. (1974) In preparation.

temperature it undergoes pyrolysis by the reaction:<sup>13</sup>



The tetrafluoroethylene intermediate  $C_2F_4$  is the same compound that results from Teflon TFE decomposition. In a shock-heated mixture containing Freon 114B2 as well as oxygen, the original compound is totally destroyed at temperatures in excess of 1144°K, yielding oxidation products similar to those of Teflon oxidation. In the electrophilic experiments, the dissimilarity of chemistries—the addition of bromine in the case of Freon 114B2—is so slight that the efficiency of liquid injection versus solid ablation can be compared.

### 5. ANTENNA MEASUREMENTS

In discussing the antenna measurements made during the flight, we first define the specific antenna system properties that are to be considered in the analysis of the flight data. We then present the low-power test system instrumentation and the flight test results for that system, followed by the high-power test system and the telemetry system. The phenomena involved are antenna impedance mismatch, interantenna coupling, signal attenuation, voltage breakdown, and pulse shape distortion.

Impedance mismatch effects are most easily obtained by monitoring the incident power  $P_{inc}$  and the reflected power  $P_{ref}$  at the terminals of an antenna. The power reflection coefficient  $R$ , defined

$$R = \frac{P_{ref}}{P_{inc}}, \quad (1)$$

is a good indication of the operation of the antenna. The power reflected from an initially matched antenna increases as the plasma density increases.

The power received by a second antenna located near a transmitter is also greatly influenced by the plasma sheath. The substantial reduction in received power  $P_{rec}$  in the presence of the plasma sheath is due to: (1) the rise in the reflection coefficient of the transmitting antenna so that only part of the incident power is radiated; (2) the increase in attenuation of the transmitted signal as it propagates to the receiving antenna. The interantenna coupling loss (ICL) is defined as

13. Skinner, G. B., and Ringrose, G. H. (1965) Shock-tube experiments on inhibition of the hydrogen-oxygen reaction, J. Chem. Phys. 43(No. 11):4129-4133.

$$ICL = 10 \log \frac{P_{inc}}{P_{rec}}, \quad (2)$$

and includes both internal reflection losses and external attenuation losses. The external coupling loss (ECL) is obtained from Eq. (2) by subtracting out the reflection loss according to the rule

$$ECL = 10 \log \left( \frac{P_{inc} - P_{ref}}{P_{rec}} \right). \quad (3)$$

The signal power  $P_g$  finally received at a ground receiver is also greatly reduced by the ionization. This is due to a number of causes: (1) as before, a reduction in transmitted power due to antenna mismatch; (2) the large increase in attenuation (above the freespace value) caused by the plasma; (3) a variation often produced by a modification in the antenna pattern itself induced by the ionization. The total signal attenuation (TSA) is defined relative to the freespace value as:

$$TSA = 10 \log \left[ \left( \frac{P_{inc}}{P_g} \right) \left( \frac{P_g}{P_{inc}} \right)_o \right] \quad (4)$$

where  $10 \log \left( \frac{P_g}{P_{inc}} \right)_o$  is the minimum value of attenuation during a spin cycle measured before plasma effects become important.

It is often desirable to separate the effect of antenna mismatch from the values obtained for TSA, and so the composite signal attenuation (CSA), defined as

$$CSA = 10 \log \left[ \left( \frac{P_{inc} - P_{ref}}{P_g} \right) \left( \frac{P_g}{P_{inc}} \right)_o \right]. \quad (5)$$

has been introduced.

All of the quantities considered so far vary as the sensing antenna rotates during reentry. The data for these quantities must therefore always be presented as a function of spin angle or for a specific vehicle orientation, such as windward or leeward.

An additional consideration with regard to the high-power test system is antenna voltage breakdown. Breakdown is indicated by a sharp rise in the reflected energy, with a concomitant decrease in the received power. Because the high-power pulse can modify the plasma, it is necessary to make measurements on this system throughout the duration of the pulse. Thus, the high-power system results for R, TSA, and CSA, are determined for each selected altitude and body orientation as a function of time during the pulse.

## 5.1 S-Band Low-Power Experiment

### 5.1.1 SYSTEM DESCRIPTION

A simplified block diagram of the low-power S-band test system used in this chemical additive experiment is shown in Figure 13. The 2290.5-MHz, 2.5-W transmitter was connected to its transmitting (TX) antenna through a reflectometer made up of a directional coupler to sample the incident power  $P_{inc}$ , and a circulator to determine the reflected power  $P_{ref}$ . A four-probe reflectometer was also included to determine the phase as well as magnitude of the antenna impedance. The magnitude of the reflection coefficient determined from the four-probe reflectometer can be compared with that determined from the coupler-circulator reflectometer as an internal calibration. [Data from the four-probe reflectometer will not be included in this report but will be presented at a later time.]

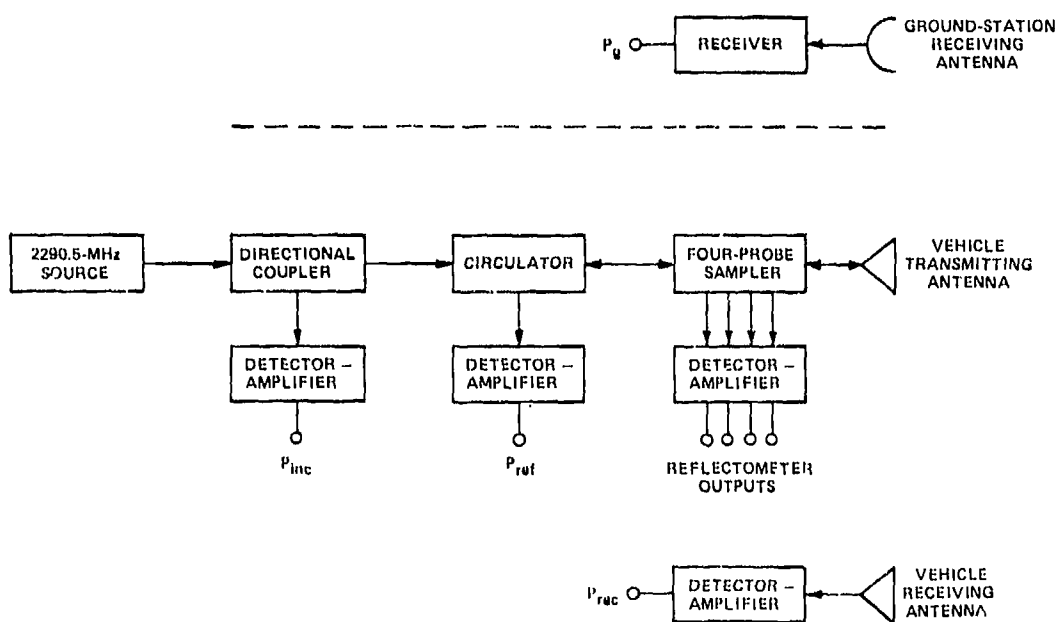


Figure 13. Low-Power Test System (simplified block diagram)

The transmitting antenna for the low-power system was located forward of the receiving antenna (Figure 14). The power coupled into the receiving antenna from the transmitting antenna  $P_{rec}$  was monitored during flight to determine the effect of the ionization and ablating Teflon on interantenna coupling. In addition to the

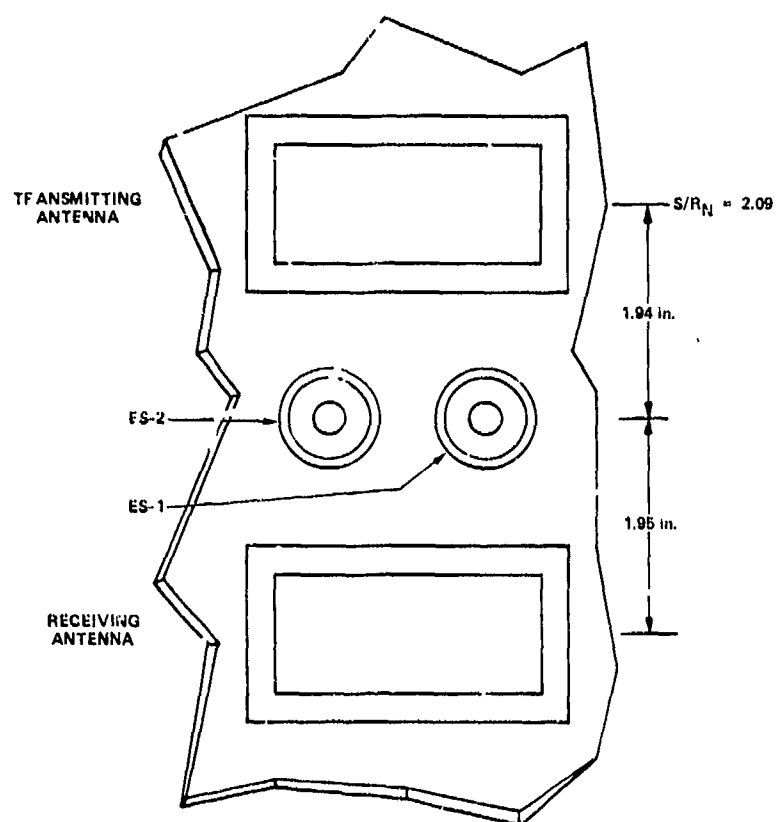


Figure 14. Sketch of Vehicle Surface Cut Away to Show Low-Power Test System

onboard measurement of  $P_{inc}$ ,  $P_{ref}$ , and  $P_{rec}$ , the intensity of the signal received on the ground  $P_g$  was continuously monitored during the flight to determine signal attenuation. These two types of measurement were also essential for establishing the vehicle spin and precession history.

#### 5.1.2 SPIN AND PRECESSION

Owing to their dependence on local properties, most onboard measurements are modulated at a frequency equal to the sum of the spin and precession rates. The signal received at the ground-based antenna varies in strength as the vehicle rotates about its longitudinal axis but is only slightly affected by the precession since the pattern of the transmitting antenna is rather broad.

The vehicle spin rate is based on the ground antenna data (Figure 15). This is used to isolate the precession rate from the total cyclic variation. The latter is determined by two distinct onboard measurements: reflectometer and electrostatic probe data. The combined ground-based and onboard data identifies the

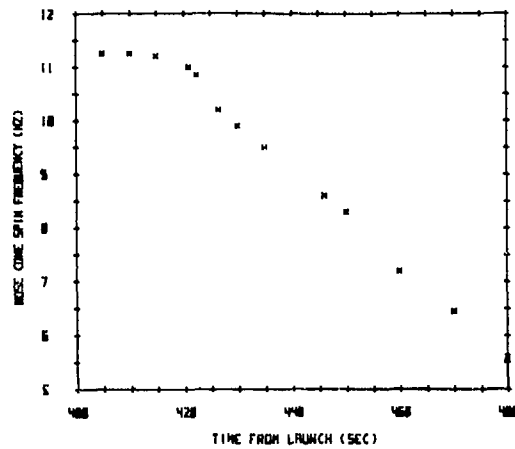


Figure 15. Nose Cone Spin Rate

spin and precession that occurred at any altitude (Figure 7), which is prerequisite to analysis of the test data.

### 3.1.3 FLIGHT TEST RESULTS

Inspection of Figure 16 shows that the power reflection coefficient  $R$  of the low-power test antenna was at first greater on the windward axis than on the leeward axis. At about 200 kft there was an abrupt decrease in the growth of the mismatch on the windward axis; on the leeward axis there was no corresponding

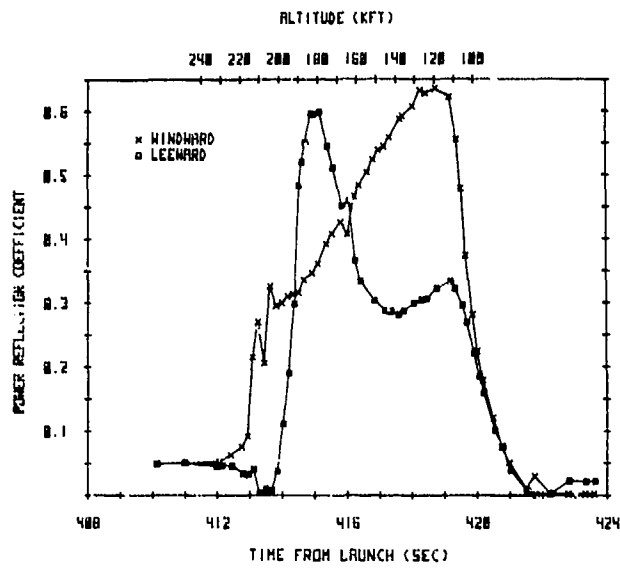


Figure 16. Low-Power Reflection Coefficient

decrease. At about 190 kft the reflection coefficient on the leeward axis became the greater; at about 165 kft it again became the smaller. At 100 kft the angle of attack had decayed considerably, and the reflection coefficient ceased to vary with spin.

The response of the test antenna can be evaluated by comparing reflection data with that obtained in the earlier experiments that were conducted without chemical additives, when the peak value of the reflection coefficient for the bare body was  $R = 0.9$ , and the response on the windward axis was always greater than on the leeward axis. On the fifth flight, with additives, the peak value was  $R = 0.6$ ; and the response depended on the mixing of the ablating Teflon and the depth and extent of the air flow modified thereby, which in turn depended on the body orientation and angle of attack.

Figures 17(a) through (g) show the reflection response of the low-power test antenna to the plasma as a function of spin angle. Over the altitude range from 200 to 100 kft the pattern varies greatly with spin.

At 200 kft [Figure 17(a)] the minimum reflection occurs on the leeward axis but conditions change so rapidly that the value at successive leeward positions increases from one spin cycle to the next. The maximum reflection ( $R = 0.3$ ) actually occurs when the antenna is midway between the leeward and windward positions.

At 190 kft [Figure 17(b)] the reflection coefficient is greater on the leeward axis than on the windward axis. The value continues to increase at successive leeward positions, and the position of maximum reflection shifts away from the windward axis toward the leeward axis.

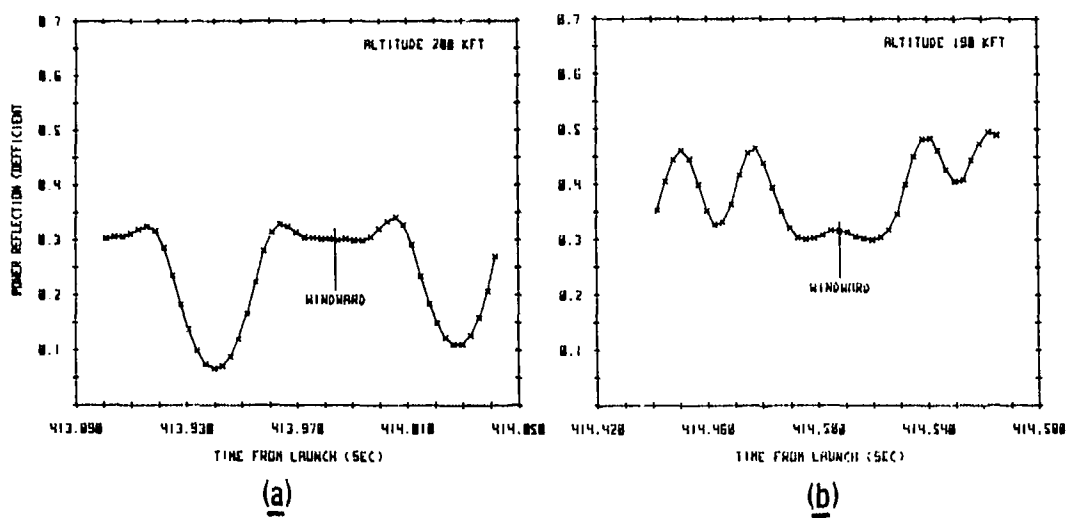
At 180 kft [Figure 17(c)] the pattern shape again changes, markedly. Now there are distinctive peaks on the leeward axis and a secondary, much smaller, peak on the windward axis.

At 170 kft [Figure 17(d)] the reflection coefficients corresponding to the leeward and windward axes are nearly equal. The minimum values occur for body positions midway between them.

At 160 kft [Figure 17(e)] the pattern shape again changes. Now the response on the leeward axis is greatly suppressed and the peak value clearly occurs on the windward axis, the minimum value occurs between the two.

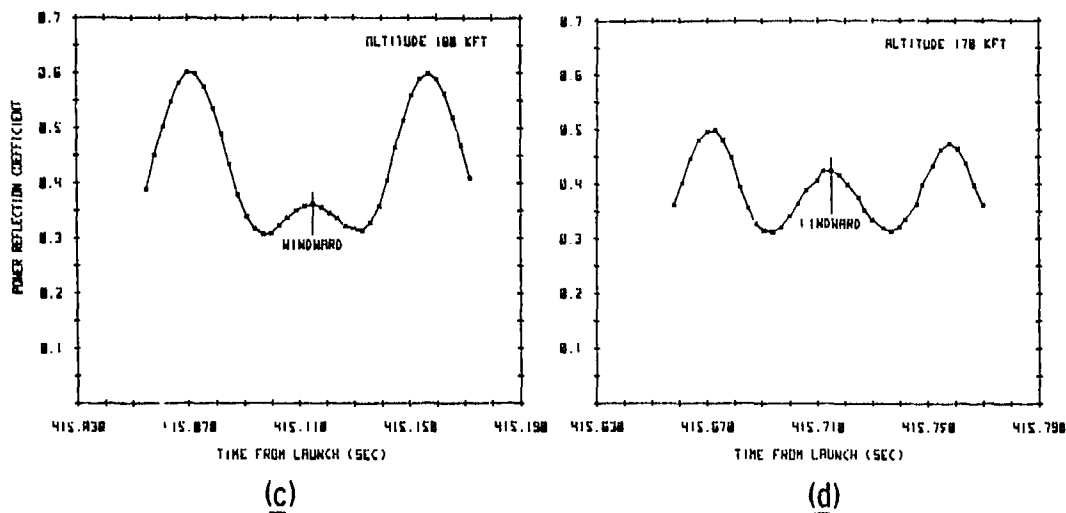
The shape of the curve does not change markedly over the next 50 kft; there is still the peak on the windward axis and the continuing trend toward the minimum on the leeward axis, with no secondary peaks at intermediate points. The behavior at 140 kft [Figure 17(f)] continues down through 110 kft.

Below 110 kft there is a sudden change in the pattern and the variation with spin disappears [Figure 17(g)]. The reflection coefficient steadily decreases and returns to its ionization-free value at around 90 kft.



(a)

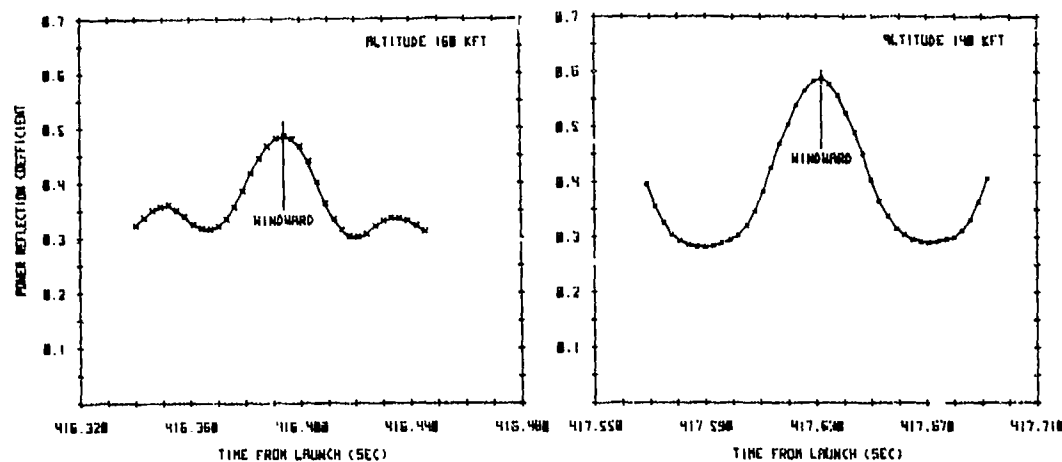
(b)



(c)

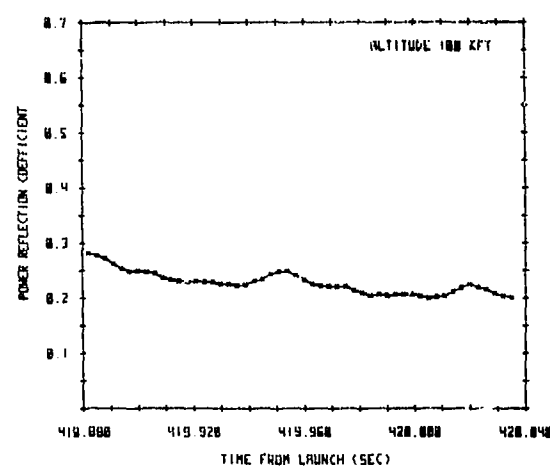
(d)

Figure 17. Variation in Low-Power Reflection Coefficient During One Spin Cycle [(a) 200 kft, (b) 190 kft, (c) 180 kft, (d) 170 kft...]



(e)

(f)



(g)

← Figure 17. Variation in Low-Power Reflection Coefficient During One Spin Cycle [...(e) 160 kft, (f) 140 kft, (g) 100 kft]

The interantenna coupling loss, defined by Eq.(2) and plotted in Figure 18, parallels the reflection coefficient in behavior by increasing first on the windward side and then on the leeward side. At 100 kft it had increased by about 20 dB over its initial value, after which it rapidly returned to its freespace value. From 130 kft down, the leeward and windward values did not differ by more than 1 or 2dB.

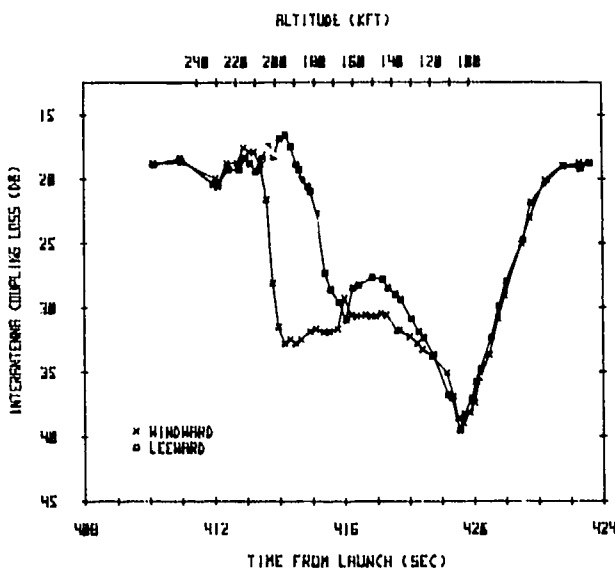


Figure 18. Interantenna Coupling Loss

The interantenna coupling varies with spin and altitude. This can be seen in Figures 19(a) through (e), which are plotted for altitudes from 200 to 100 kft.

At 200 kft [Figure 19(a)] the pattern shows a change of greater than 13 dB in interantenna coupling loss as the nose cone rotates through a spin cycle. Since the reflection coefficient was not very large at this altitude, the difference between the interantenna and external coupling losses is not great.

At 180 kft [Figure 19(b)] the interantenna coupling loss has increased for a larger fraction of the spin cycle. The maximum value occurs on the windward axis.

At 160 kft [Figure 19(c)] the variation with spin is suppressed but the overall coupling loss has increased to about 30 dB.

At 120 kft [Figure 19(d)] there is a further increase of between 2 to 4 dB in the coupling loss.

At 100 kft [Figure 19(e)] the coupling loss is greatest (almost 38 dB) but there is almost no variation with spin.

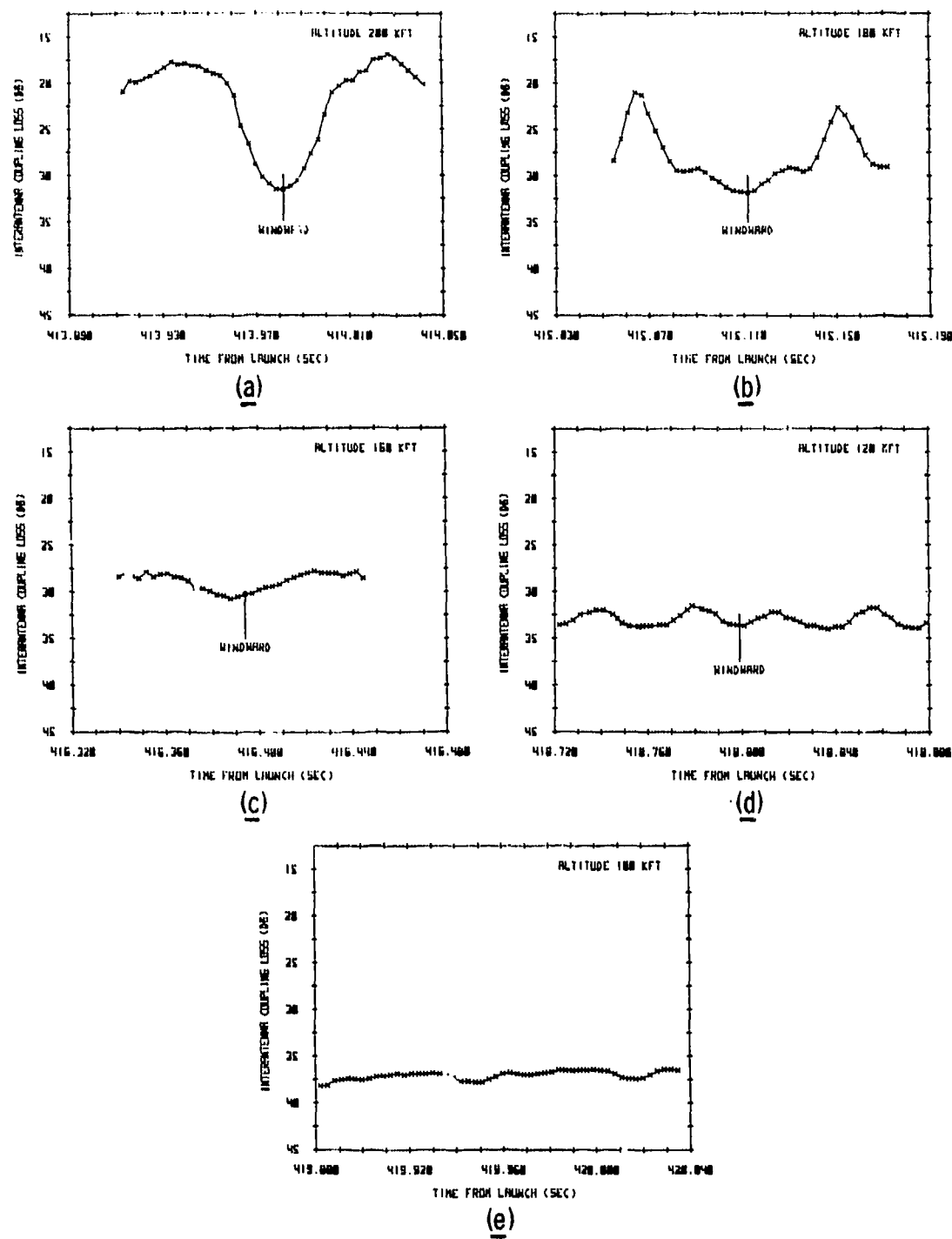


Figure 19. Variation in Low-Power Interantenna Coupling Loss During One Spin Cycle [(a) 200 kft, (b) 180 kft, (c) 160 kft, (d) 120 kft, (e) 100 kft]

The signal received on the ground varies as the vehicle spins. The TSA defined in Eq. (4) is plotted in Figures 20(a), (b), and (c), where each of the data points corresponds to the attenuation at the instant of peak received signal on the ground during a spin cycle.

The data for Figure 20(a) was obtained from the main base ADAS tracker. At about 200 kft it shows a sharp increase in attenuation which was concurrent with significant increase in R and ICL. After this initial rise the attenuation gradually increased, down to 120 kft, where it began steadily decreasing back to freespace values.

The curves in Figures 20(b) and 20(c) show the signal attenuation based on data obtained from the main base medium gain tracker (MGT) and the Coquina Beach tracker, respectively. The slight decrease in attenuation early in reentry is typical of all flights, the result of an increase in the gain of the nose cone transmitting antenna caused by narrowing of the radiation pattern.

## 5.2 High-Power Test System

### 5.2.1 SYSTEM DESCRIPTION

A simplified block diagram of the high-power test system is shown in Figure 21. The transmitter for this system operated at 2255.5 MHz and had a peak power of 1 kW, producing a 3- $\mu$ sec pulse at a prf of 160 pps. It was connected to its antenna through a reflectometer, which monitored the incident and reflected power levels.

The bandwidth of the telemetry system was much too small to accommodate the frequency components of a 3- $\mu$ sec pulse, and so airborne measurement of the pulsed signal was somewhat indirect: only the average value of incident power was measured and transmitted to the ground. The peak incident power was computed from this on the assumption that there was no change in the shape of the incident pulse during the flight.

Measurement of the reflected pulse was more involved because of interaction between the high-power signal and the ionized air during pulse on-time. To observe the changes that occurred in the reflected signal in the course of a single pulse, the amplitude was sampled four times during the pulse. Transmission of these four values to the ground involved only low-frequency data since the sampling was done at the transmitter prf. The approximate shape of each reflected pulse was reconstructed from the four samples of that pulse.

The sketches in Figure 22 represent (top) an ideal incident pulse and (bottom) a typical reflected pulse. The four X's on the lower curve indicate the times at which the reflected pulse was sampled. In this reconstruction the reflection coefficient R is arbitrarily held at the final sample value until just before the end of the sampling interval.

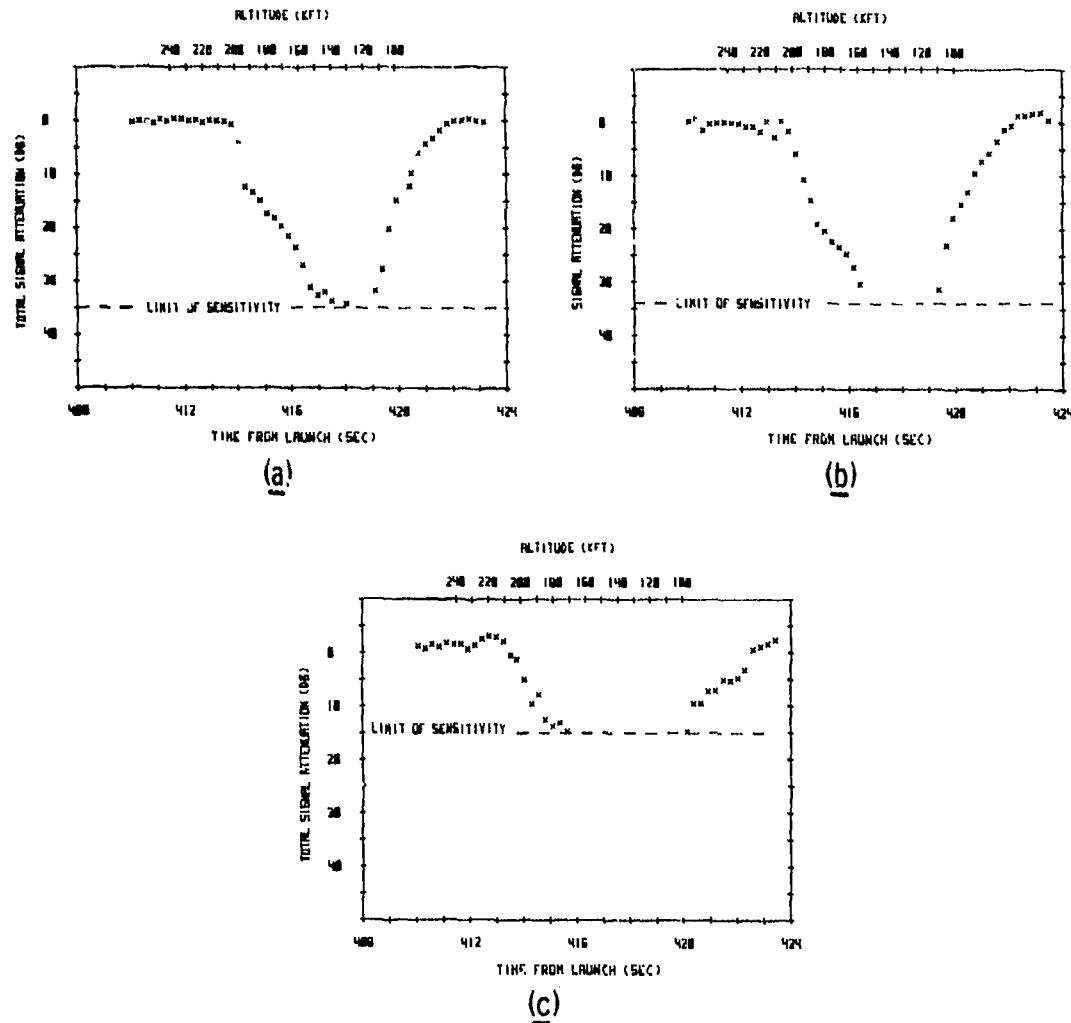


Figure 20. Total Signal Attenuation (Low Power) [(a) ADAS Data, (b) Main Base MGT Data, (c) Coquina Beach MGT Data]

At each ground receiving site, photographs were made of the received high-power pulses displayed on calibrated oscilloscopes. These were read in conjunction with records of the receiver AGC voltage to extract details of the intrapulse variation in received signal intensity. A more complete analysis of the data from the ground receiving stations will be presented in a subsequent report.

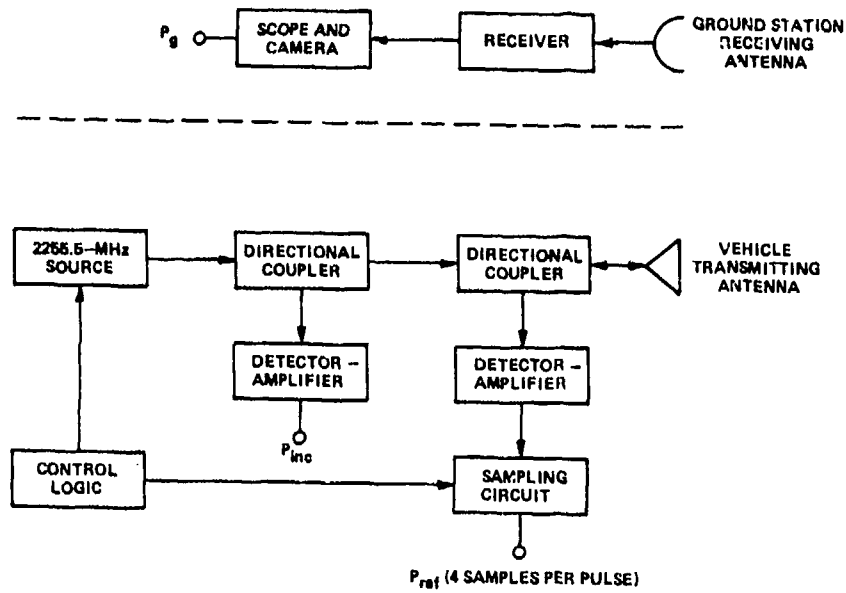


Figure 21. High-Power Test System (simplified block diagram)

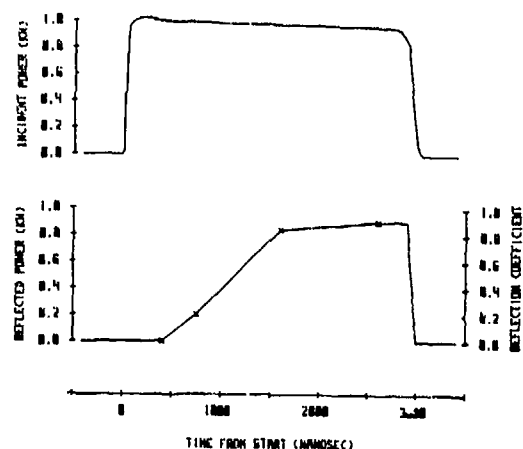


Figure 22. Typical High-Power Incident and Reflected Pulses (sampling times marked X)

### 5.2.2 FLIGHT TEST RESULTS

The reflection coefficient  $R$  on the windward axis of the high-power transmitting antenna is presented in Figure 23(a). Four curves are shown, one for each of the sampling times specified in Figure 22. They differ from the corresponding low-power reflection coefficient displayed in Figure 16 in two respects. First, the peak value of the reflection coefficient is much larger than that for the low-power system. This is not unusual, especially at the higher altitudes, because of nonlinear effects such as antenna breakdown. Second, the magnitude of  $R$  generally increases with each succeeding sample within a pulse. This occurs since the high-power pulse produces an increase in ionization and a corresponding increase in antenna mismatch.

The reflection coefficient  $R$  on the leeward axis [Figure 23(b)] is similar to that on the windward axis but begins to increase later and decay toward the free space value sooner. The maximum value of  $R$  is about the same on both sides and, except at altitudes above 200 kft, the variation of  $R$  with spin is small.

One important difference between the high-power reflection coefficients on the windward and leeward axes is that in the data for the latter there are some local minima. This type of response was often observed in data from the low-power antennas on no-additive flights,<sup>14</sup> and was shown to be due to the nonmonotonic response of the antenna to increasing electron concentration. In the present case the analysis is more complicated because the presence of additive in the three-dimensional cross flow results in asymmetric mixing variations that influence the antenna response.

The variation of the reflection coefficient  $R$  during the course of a pulse is presented in Figure 24 for five series of pulses at altitudes from 236 to 190 kft. Each row represents responses observed during one spin cycle. A straight line along the abscissa indicates no reflection. On each miniplot (greatly expanded in width) the center corresponds to the angular position of the transmitting antenna at the instant the pulse was transmitted.

For purposes of this preliminary report, any sharp change in the reflection coefficient  $R$  at successive sampling times within a pulse has been considered evidence (although not completely definitive) of antenna breakdown. According to this criterion, breakdown occurred at altitudes as high as 236 kft but only on the windward axis. At 200 kft, a strong reflected pulse was observed over the entire spin cycle, although the intrapulse variation of  $R$  was small except toward the leeward axis. Below 190 kft, the variation of  $R$  within a pulse remained small, and was almost independent of spin angle. The amplitude of the reflected power gradually decreased.

14. Lennon, John F., and Poirier, J. Leon (1974) Interpretation of Microwave Antenna Results from a Reentry Flight Test: A Comparison of Methods, AFCRL-TR-74-0389.

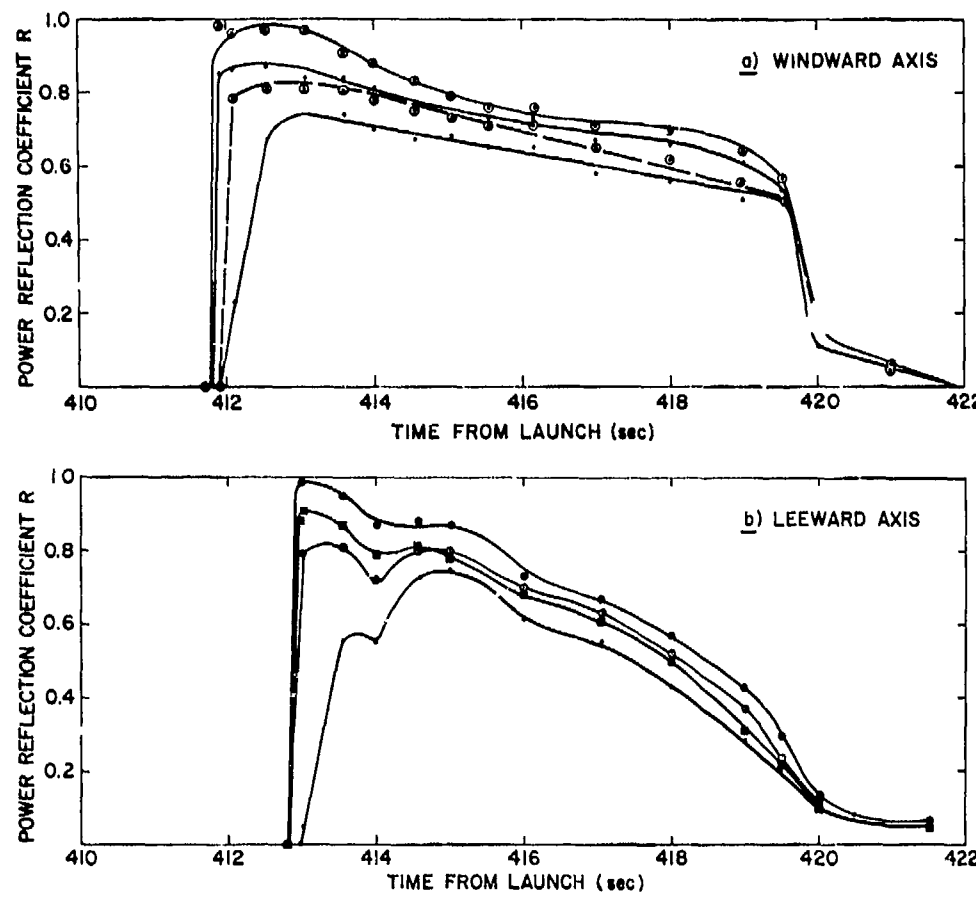


Figure 23. High-Power Reflection Coefficient [(a) windward axis, (b) leeward axis]

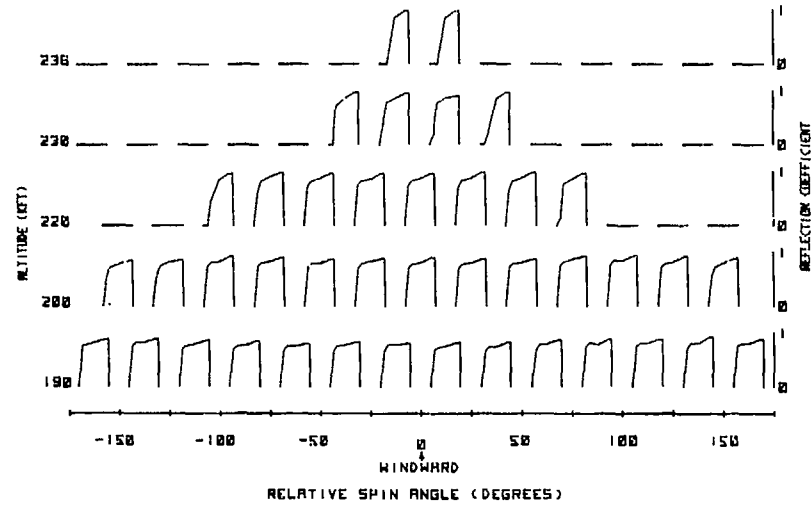


Figure 24. High-Power Reflection Coefficient at Selected Altitudes

The observed onset of breakdown can be compared with predicted values by referring to Figure 25, where the power required for breakdown as measured in the laboratory is plotted as a function of pressure. The equivalent values for the altitude scale were obtained from the computations plotted in Figure 26 for the zero angle-of-attack boundary-layer pressure at the shoulder as a function of altitude. Since the maximum transmitter power is only slightly over 1 kW, it is apparent from Figure 25 that the onset of breakdown should

Figure 25. Power Required for Antenna Breakdown (laboratory experiment; zero angle of attack)

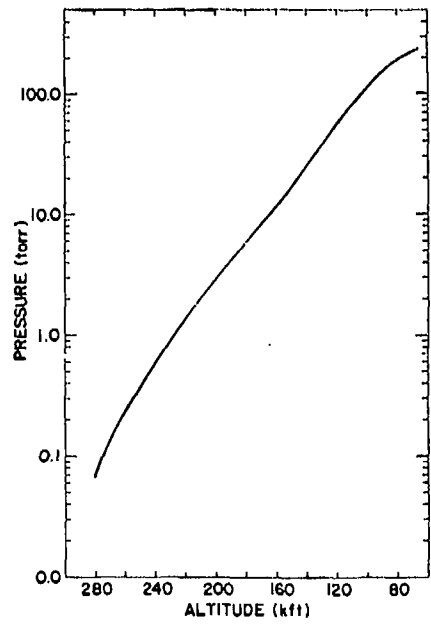
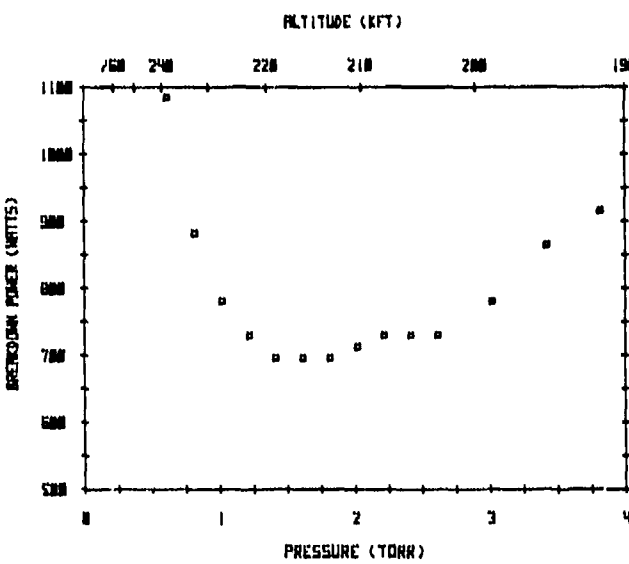


Figure 26. Computed Boundary-Layer Pressure at the Shoulder

occur at 240 kft. If the effect of angle of attack is included in the computations of boundary-layer pressure, the altitude for the predicted onset of breakdown is raised by about 10 kft. Figure 24 shows that breakdown was first observed at 236 kft. Although the data from this experiment has not been completely analyzed, and no data on breakdown in the absence of additives is available for direct comparison, there is nevertheless sufficient evidence to infer that Teflon acted to delay the onset of breakdown.

Establishing the lower altitude bound for the occurrence of nonlinear effects is not easy, but one approach is to compare the low-power and high-power reflection coefficients on the windward [Figure 27(a)] and leeward [Figure 27(b)] axes. A number of observations can be made. The onset of the response on the high-

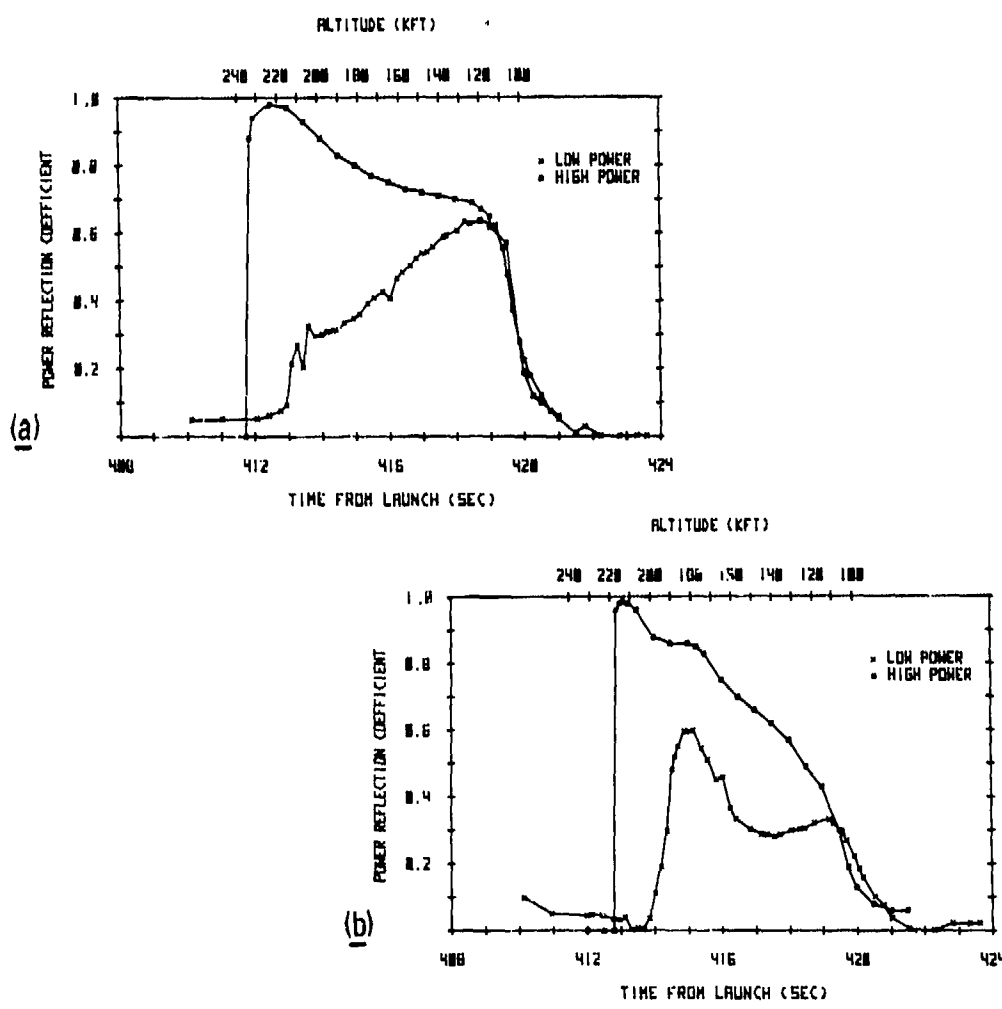


Figure 27. Comparison of High- and Low-Power Reflection Coefficients [(a) windward, (b) leeward]

power system occurred at a higher altitude than it did on the low-power system. The difference in altitude between the two was about 20 kft. The maximum value of  $R$  was much larger on the high-power antenna for all altitudes above 120 kft. Below this point, the responses of the two systems were similar.

### 5.3 Secondary S-Band Test/TM System

#### 5.3.1 SYSTEM DESCRIPTION

The telemetry system was a standard 5-W FM/FM system that operated at a frequency of 2220.5 MHz. The transmitter was connected to a set of four circumferential slot antennas equispaced around the nose cone through a tree of three coaxial matched power dividers. The antennas were cavity-backed slots filled with boron nitride; the dimensions of the cavity were  $1.164 \times 2.437 \times 0.874$  in. deep. To minimize the effects of the plasma, the antennas were mounted far back on the nose cone (Figure 2).

Figure 28 is a simplified block diagram of the telemetry system. For the secondary test system, one of the telemetry antennas was connected to its power divider through a reflectometer consisting of a directional coupler and a circulator. The reflectometer output, an indicator of the operation of the TM/TX antenna, was subsequently transmitted back to earth over the telemetry link.

As a precaution against degradation of the telemetry system performance by an unequal division of power among the four antennas, isolators were used at

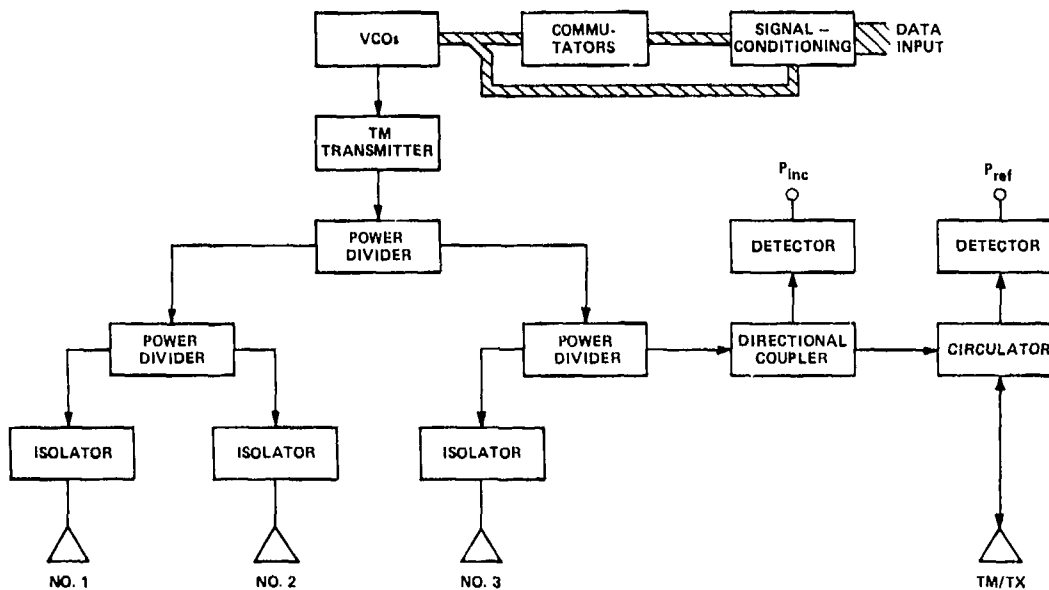


Figure 28. Telemetry/Secondary Test System (simplified block diagram)

each telemetry antenna input. These presented unequal mismatches at the antennas from redistributing the power within the power-divider tree. The variations in mismatch resulted from effects of the angle of attack on the plasma distribution about the vehicle.

### 5.3.2 FLIGHT TEST RESULTS

The pattern of the reflection coefficient  $R$  for the TM/TX antenna is shown in Figure 29. Because this antenna was at the rear of the nose cone, where the level of ionization was lower than at the shoulder where the test antenna was located, its response occurred at a lower altitude. Initially, the responses on the leeward and windward axes were similar. Shortly after onset there was a sharp decrease in the value of  $R$  on the leeward axis; the windward response increased, rising to almost 0.3. At about 160 kft the leeward value began to rise. Below about 150 kft it peaked at close to 0.5, while the windward value went slightly above 0.3. Both then described practical parallel courses down to the initial value.

The complex relationship between the instantaneous antenna nose cone orientation and the effectiveness of the ablating Teflon in suppressing the rise in reflection coefficient is further emphasized by the curve for the maximum value of  $R$  in Figure 29. This curve is a plot of the largest value of reflection coefficient observed during each spin cycle. Between 190 and 150 kft the position of the maximum reflection corresponds to neither the windward nor the leeward axis.

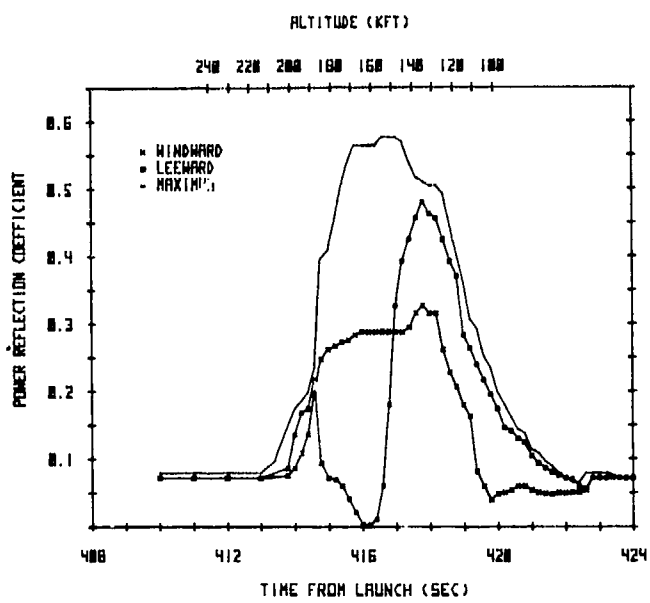


Figure 29. Power Reflection Coefficient of TM/TX Antenna

The TSA is plotted in Figure 30. Three sets of data are shown here. One set was obtained from the ADAS telemetry receiving system on Wallops Station. The other two are the right- and left-hand polarization components of the signal received by the medium gain tracker of the telemetry (MGT) receiving system which was also located on Wallops Station.

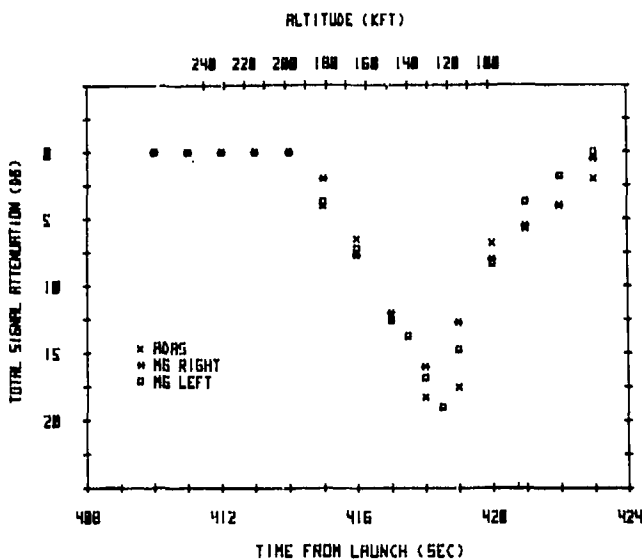


Figure 30. Total Signal Attenuation Measured by Main Base MGT and ADAS

## 6. ELECTROSTATIC PROBE DATA ANALYSIS

### 6.1 General Description of Probes

In the fifth Trailblazer flight test the nose cone carried eight electrostatic probes, more than used in any of the previous flight tests. The presence of negative ions produced by the attachment of electrons to molecules coming into the flow from the ablation of Teflon made it impossible to assume that the electron density was equal to the ion density. Five of the probes were therefore biased positive to measure the electron density directly.

The probes were identical with those flown on the third and fourth Trailblazer flight tests.<sup>2,3</sup> Each consisted of a flushmounted 1/4-in.-dia. gold-plated copper electrode isolated from the rest of the vehicle surface by lava dielectric material (Figure 31). The probes were capable of measuring charged particle densities over a four-decade range, and contained circuitry for automatic temperature compensation and preflight calibration.

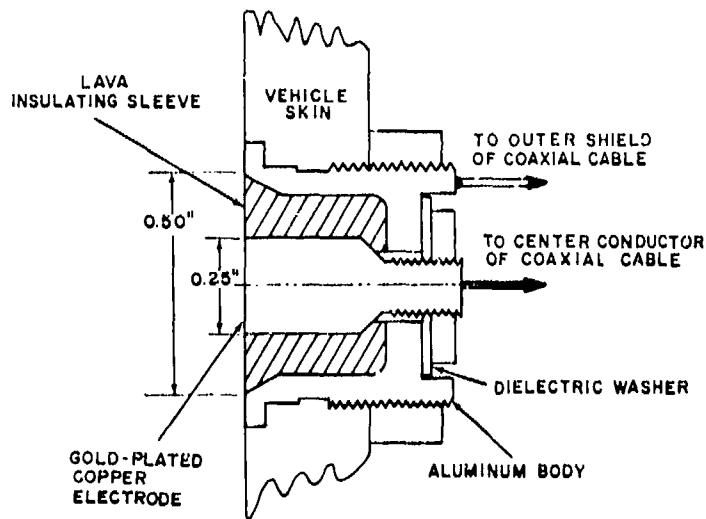


Figure 31. Cross-Sectional View of ES Probe Assembly

## 6.2 Theory

A detailed discussion of electrostatic probe theory has already been presented in earlier reports<sup>1-3</sup> on Trailblazer flight tests. Here it is necessary to give only a brief description of the technique used in analyzing the probe data.

In most of the altitude regime of interest, the charged particles passing through the probe sheath region to the collecting surface undergo a considerable number of collisions with neutral particles. The probes were therefore biased at  $|V| \geq 15V$ . Experience<sup>15</sup> has shown this level to be high enough to cause the bulk of the collisions to result in forward scatter, minimizing scattering out of the sheath region and consequently minimizing the loss in probe current. It has therefore been assumed that the full random flux of ionized particles of one sign will be collected. A planar probe and a planar sheath have also been assumed.

Under these conditions the expression for the probe current is given by

$$j = (1/4) nev. \quad (6)$$

Following Bohm et al.<sup>16</sup> the electron temperature is used in calculating the ther-

- 15. Scharfman, W. E., and Bredfeldt, H. R. (1967) Experimental Studies of Electrostatic Probes for the Reentry Measurements Program, Phase B, Subcontract 611603 under Prime Contract 30-0690 AMC-333(Y), SRI Project 6138, Stanford Research Institute, Menlo Park, Calif.
- 16. Bohm, D., Burhop, E. H. S., and Massey, H. S. W. (1949) Use of probes for plasma exploration, Chap. 2 in The Characteristics of Electrical Discharges in Magnetic Fields, Guthrie, A., and Wakerling, R. K., Eds., McGraw-Hill.

mal speed

$$v = (3kT_e/m)^{1/2} \quad (7)$$

of collected particles at the sheath edge, which is derived from the planar, space-charge limited, mobility-controlled, diode equation

$$j = \frac{9}{8} \epsilon_0 \mu \frac{V^2}{\lambda^3} \quad (8)$$

Equations (6) to (8) apply only under conditions of current saturation in a two-component plasma, that is, in a plasma consisting of electrons and only one type of positive ion, with the additional constraint that the probe bias must be large enough to attract all particles of one of the species entering the probe sheath region and repel all particles of the other species.

The plasmas produced during the fourth and fifth Trailblazer flights consisted of at least three types of charged particles. In addition to positively charged particles and electrons, there were heavy, negatively charged particles. Under these conditions, Eqs. (6) and (8) do not hold when the probe is biased positive to collect negatively charged particles.

In the analysis of the data from the fourth and fifth flight tests, the effect of the negatively charged ions on the current collected by positively biased probes has been neglected in calculating the electron density. To justify this, a simple ad hoc theory of current collection in the presence of negative ions has been developed. It will be shown that for the conditions achieved during the Trailblazer additive flight tests, the negative ion contribution to the negative current can be neglected when determining the electron density, but must be included when the probe sheath thickness is determined.

First, consider Eq. (6) for the charged particle concentration as a function of the probe current. When negative ions are present, Eq. (6) becomes

$$j = \frac{n_e e v_e}{4} + \frac{n_- e v_-}{4} \quad (9)$$

From charge neutrality,

$$n_- = n_+ - n_e \quad (10)$$

Therefore, Eq. (9) becomes

$$j = \frac{n_+ e v_+}{4} + \frac{n_e e v_e}{4} \left[ 1 - \left( m_e / m_- \right)^{1/2} \right] \quad (11)$$

where it has been assumed that the electron temperature is to be used to calculate the thermal velocity of all charged particles. Solving for  $n_e$  yields

$$n_e = \frac{\frac{4j}{ev_e} - n_+ (m_e/m_-)^{1/2}}{1 - (m_e/m_-)^{1/2}} . \quad (12)$$

Assuming that the negative ion species is  $F^-$ , which is a lower bound on the negative ion mass, we find

$$(m_e/m_-)^{1/2} \approx 5.36 \times 10^{-3}.$$

Thus, this term may be neglected in the denominator and if we set

$$\frac{4j}{ev_e} = n'_e .$$

then Eq. (12) becomes

$$n_e = n'_e - (5.36 \times 10^3) n_+ . \quad (13)$$

The greatest difference between the positive ion density and the electron densities observed on both the fourth and fifth flights was approximately two orders of magnitude. Under this condition, Eq. (13) indicates that  $n'_e$  overestimates  $n_e$  by at most a factor of 2. This is within the estimated accuracy of the probe measurements (factor of from 2 to 3) and so the negative ion density may be neglected in calculating the electron density.

The prediction of the sheath thickness is another matter. To obtain an expression analogous to Eq. (8) for the sheath thickness when negative ions are present, we must start with Poisson's equation in one dimension (planar sheath):

$$\frac{d^2V}{dx^2} = -\frac{en_e}{\epsilon_0} - \frac{en_-}{\epsilon_0} , \quad (14)$$

where at any point within the sheath

$$\begin{aligned} j_e &= n_e e v_{e\mu} , & j_- &= n_- e v_{-\mu} ; \\ v_{e\mu} &= \mu_e E = -\mu_c \frac{dV}{dx} , & v_{-\mu} &= \mu_- E = -\mu_- \frac{dV}{dx} . \end{aligned} \quad (15)$$

Therefore, Eq. (14) becomes

$$\frac{dV}{dx} \frac{d^2V}{dx^2} = \frac{j_e}{\epsilon_0 \mu_e} + \frac{j_-}{\epsilon_0 \mu_-} . \quad (16)$$

Integrated, this gives:

$$\frac{9}{8} \epsilon_0 \frac{V^2}{\lambda^3} \approx \frac{j_e}{\mu_e} + \frac{j_-}{\mu_-} . \quad (17)$$

Now the current measured is the total current:

$$j = j_e + j_- , \quad (18)$$

and Eq. (17) can be rewritten as:

$$\frac{9}{8} \epsilon_0 \frac{V^2}{\lambda^3} = \frac{j_- j_+}{\mu_e} + \frac{j_-}{\mu_-} = \frac{j}{\mu_e} + j_- \left( \frac{1}{\mu_-} - \frac{1}{\mu_e} \right) . \quad (19)$$

Thus,

$$\frac{9}{8} \epsilon_0 \mu_e \frac{V^2}{\lambda^3} = j + j_- \left( \frac{\mu_e}{\mu_-} - 1 \right) . \quad (20)$$

Assuming total charge neutrality,

$$j_- = \frac{n_- e v_-}{4} = (n_+ - n_e) \frac{e v_-}{4} , \quad (21)$$

and Eq. (20) becomes

$$\frac{9}{8} \epsilon_0 \mu_e \frac{V^2}{\lambda^3} = j + \frac{e v_-}{4} \left( \frac{\mu_e}{\mu_-} - 1 \right) (n_+ - n_e) . \quad (22)$$

If the second term on the righthand side of Eq. (22) is much smaller than the first, which represents the negative current density measured at some time during reentry, the negative ions can be neglected in determining the sheath thickness. This is not the case here, as demonstrated by the following rough calculation based on data from the fourth flight.

The mobility is estimated by using expressions derived from kinetic theory:

$$\frac{\mu_e}{\mu_-} = \frac{m_- \nu_{-N}}{m_e \nu_{eN}} = \frac{m_- \sigma_{-N} V_-}{m_e \sigma_{eN} V_e} = \left( \frac{m_-}{m_e} \right)^{1/2} \frac{\sigma_{-N}}{\sigma_{eN}}. \quad (23)$$

With  $F^-$  again assumed to be the negative ion present, and cross section values

$$\sigma_{-N} = \sigma_{NO^+N} = 1.3 \times 10^{-18} \text{ cm}^2,$$

$$\sigma_{eN} = 3.54 \times 10^{-20} \text{ cm}^2,$$

with  $T = 10^3 \text{ }^\circ\text{K}$ , Eq.(20) becomes

$$\frac{9}{8} \epsilon_0 \mu_e \frac{\Delta V^2}{\lambda^3} = 1 + 4.38 \times 10^{-12} (n_+ + n_e) = I + f(I_-), \quad (24)$$

where  $I = jA$ , and  $A$  is the area of the probe.

The fourth-flight data that is being used to compare the relative size of the two terms on the righthand side of Eq.(24) was taken from a pair of probes located at  $S/R_N = 2.40$ . The electron density was at all times at least an order of magnitude less than the ion density, and sometimes it decreased to a value two orders of magnitude less than the ion density. Table 5 lists typical flight data from these probes, along with the values of the two quantities on the righthand side of Eq.(24). In both cases it is seen that the effect of the negative ions cannot be neglected; it is actually the dominant factor. Equations (19) and (20) should therefore take the following forms:

$$\frac{9}{8} \epsilon_0 \frac{V^2}{\lambda^3} = \frac{j_e}{\mu_e} + \frac{j - j_e}{\mu_-} \quad (19')$$

and

$$\frac{9}{8} \epsilon_0 \mu_- \frac{V^2}{\lambda^3} = j - j_e \left( 1 - \frac{\mu_-}{\mu_e} \right). \quad (20')$$

Table 5. Comparison of Calculated Negative-Ion Current and Measured Total Probe Current

Time from Launch (sec)	Electron Density ( $\text{cm}^{-3}$ )	Ion Density ( $\text{cm}^{-3}$ )	Probe Current I ( $\text{A}$ )	Calculated Negative Ion Current Factor $f(I_-)$ ( $\text{A}$ )
411.6	$1.2 \times 10^8$	$2.4 \times 10^{10}$	$4.0 \times 10^{-5}$	$1.1 \times 10^{-1}$
412.2	$1.0 \times 10^{10}$	$1.8 \times 10^{11}$	$3.0 \times 10^{-3}$	$7.8 \times 10^{-1}$

It has been shown that the effect of the negative ions may be neglected (to within a factor of 2) in determining the electron density but must be included when the sheath thickness is to be determined, in which case Eq.(20') should be used. The accuracy to which the electron density has been calculated sets the limit for neglecting the second term on the righthand side of Eq.(20'). Under conditions where the electrophilic additive exerts a strong effect, the negative ion and electron currents are roughly equal [Eq.(13) and following]. Therefore, since the sheath size depends on the cube root of the righthand side of Eq.(20'), neglecting the term containing  $j_e$  will not greatly affect it.

### 6.3 Rationale of Probe Location

Eight electrostatic probes were installed on the nose cone of the reentry vehicle (Figure 2 and Table 1). There were none on the nosecap, which was covered by the Teflon ablation material. Each of three pairs of positive-biased/negative-biased probes was located in the vicinity of one of the microwave antennas carried on the flight. Probes ES-4 and ES-5 were at  $S/R_N = .77$ , just forward of the transmitting high-power test antenna (TXII, at  $S/R_N = 2.09$ ). Probes ES-1 and ES-2 were at  $S/R_N = 2.40$ , between the pair of antennas (one low-power transmitting at  $S/R_N = 2.09$ , and the other receiving at  $S/R_N = 2.71$ ) on the side of the vehicle away from the high-power transmitting antenna. Probes ES-7 and ES-8 were at  $S/R_N = 4.44$  at the same station as the telemetry antennas, just beside the secondary test antenna.

Equation (8) predicts that the sheath thickness depends on the voltage applied to the probe. Thus, varying the bias on a probe should make it possible to measure the charged-particle density at different penetration depths in the flow field. As on the third and fourth Trailblazer flights, probe ES-1 was biased +15V and +30V, and probe ES-2 was biased -15V and -30V. The other two pairs were biased at 15V, one probe in each pair held at +15V, the other at -15V.

On the fourth flight, liquid additive had been injected into the flow field from a single station on the vehicle. To measure the spread of the additive and its effects as it proceeded back along the vehicle and reacted with the flow, probes had been located at several positions on the vehicle.

On the fifth flight, the nosecap was covered with Teflon. Owing to the non-zero angle of attack, it was predictable that the Teflon reaction time from the stagnation point to the end of the Teflon-covered surface would be shorter on the windward side than on the leeward side but that the average over a complete rotation cycle would be similar at any station. To anticipate the possibility of non-uniform ablation, probes ES-3 and ES-6 were located at  $S/R_N = 2.40$ , at the same station as, and roughly equidistant from, probes ES-1 and ES-2, but on the same side of the vehicle as probes ES-4 and ES-5.

#### 6.4 Probe Results

In this section we present the complete data for each probe as functions of altitude and time from launch. As in the fourth flight, the pressure and temperature in the boundary layer necessary for calculating the charged-particle density as a function of probe current were obtained from calculations for the first three Trailblazer II flight tests.<sup>10</sup>

On the fourth flight, one probe (biased -15V) had been located at  $S/R_N = 1.77$ , the same body station as the liquid-additive injection port but displaced by  $90^\circ$ . The response of this probe was therefore unaffected by the additive and so the charged-particle density measured in this unperturbed region could be used as a standard against which to compare the results of the other probes. Since the combined effect of the spin and nonzero angle of attack of the reentry vehicle produces an almost sinusoidal modulation of the probe current, the unperturbed probe on the liquid-additive flight could also be used as a time reference to determine when the probes influenced by the additive were on the windward or leeward sides of the vehicle.

On the fifth flight, all the probes were collecting current from an ionized flow field containing Teflon ablation products, and so there was no unperturbed probe with which the others could be compared. This was not a problem since conditions of the fifth flight were similar to those of the fourth. The difference in angle of attack and reentry velocity was not such that the charged-particle densities in the fifth flight could have been more than twice those in the fourth flight.<sup>17</sup> This being within the probe error bounds anticipated, the data from the unperturbed probe of the fourth flight has been used as a reference for analyzing the probe data from the fifth flight. The ion density derived from the current measured by this probe is shown as a function of altitude in Figure 32.

##### 6.4.1 PROBES ES-4 AND ES-5 ( $S/R_N = 1.77$ )

Probe ES-4 biased at +15V, and probe ES-5 biased at -15V, sampled the plasma just in front of the high-power antenna located at  $S/R_N = 2.09$ . Figure 33 shows the data from these probes. The -15V probe became sensitive to the positive-ion density at about 270 kft (411.5 sec). Data is missing from the positive-ion curve (ES-5) late in the flight (420.0 to 422.0 sec) because the probe saturated.

There were four other short periods earlier in the flight (412.0, 414.0, 415.0, 419.0 sec) when data was apparently lost. All the results presented here were obtained from a computer compilation of the raw data. Direct examination of this

17. Lew, H. G. (1974) Angle-of-Attack Effects on Electron Density Distribution Over Blunt Bodies, AFCRL-TR-74-0354, Contract No. F19628-72C-0070, General Electric (Doc. No. 74 SD 2113).

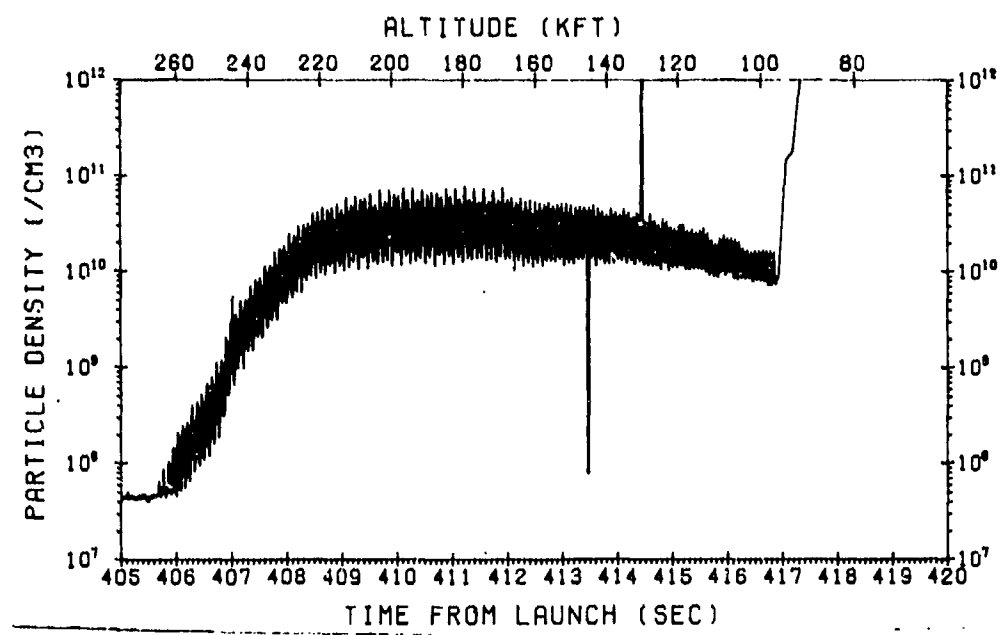


Figure 32. Unmodified Positive-Ion Density Measured at  $S/R_N = 1.77$  on Fourth Flight (probe ES-1, biased -15V)

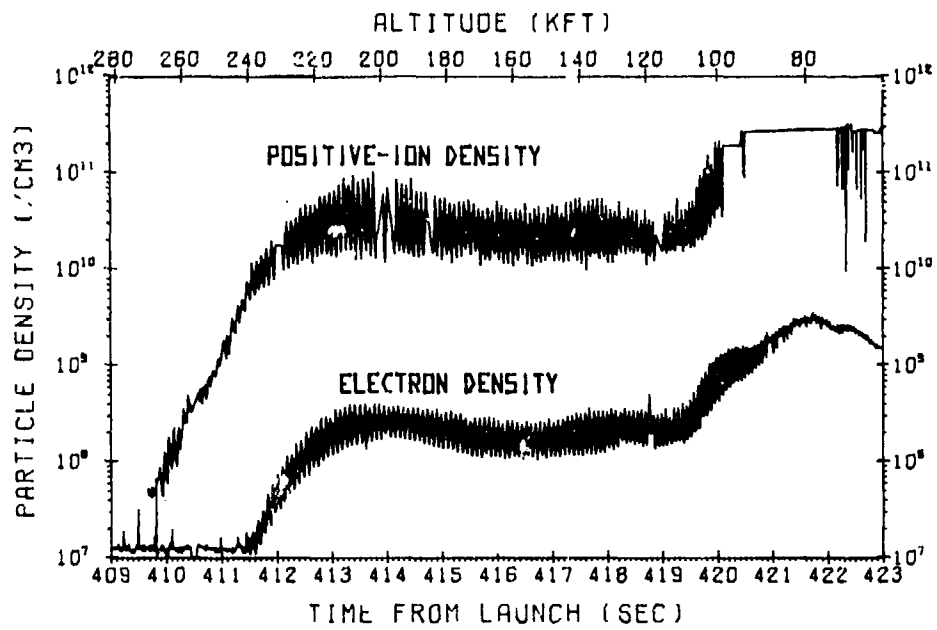


Figure 33. Charged-Particle Densities Measured at  $S/R_N = 1.77$  on Fifth Flight (probes ES-4, biased +15V; ES-5, biased -15V)

raw data shows no loss of data at the corresponding times, so the problem must lie with the computer compilation technique. Since the time span of the missing data is short and is not essential to the probe analysis, we are neglecting the missing data. As will be seen later, the same loss of data was apparent in the response of probe ES-2, which was located on the same commutator as ES-5.

The first thing noticed in Figure 33 is that the electron density is always at least two orders of magnitude less than the positive-ion density. The positive-ion density rose to a peak value of  $10^{11}$  part./cm<sup>3</sup> at approximately 210 kft, when the electron density was at its peak value of  $4 \times 10^8$  part./cm<sup>3</sup>.

The buildup of the ion density to its peak value and the ensuing plateau were compared with corresponding clean-air data from the probe on the fourth flight (Figure 32). Agreement is quite adequate. Hence, it must be concluded that the Teflon ablation products in the flow lowered the electron density without significantly cooling the ionized gas. Had cooling been important on the fifth flight, the enhanced rate of recombination of positive ions and electrons would have resulted in a lower ion density.

We now examine the effect of the spin of the vehicle and its nonzero angle of attack on the amplitude of the modulation of the charged particle densities. On the fourth flight (Figure 32) the density had varied by about a factor of 5 from windward to leeward; the amplitude of the modulation remained fairly constant until late in the flight, when the angle of attack decreased owing to atmospheric effects. On the fifth flight (Figure 33) the modulation of the electron density was similar, remaining fairly constant at a factor of 3, but this trend was not seen in the positive-ion density. At the beginning (~410.0 sec) the probe response was modulated by a factor of 3, but in the period from 410.5 to 411.2 sec there was no apparent variation. After modulation returned it increased to as much as a factor of 8 at 413.6 sec, with a subsequent decrease to 3 at 415.0 sec, where it remained constant. The loss of modulation at low altitudes could not be seen in the response of this probe owing to saturation of the probe current after 420 sec. The initial loss at high altitudes (260 to 240 kft) cannot be explained with certainty. Since the same effect was observed in the data from all probes sensitive to the plasma during this altitude regime, it may be that the initiation of Teflon ablation introduced random effects.

It will be noted in Figure 33 that both probes show an increase in charged particle density at slightly below 120 kft (419 sec). This increase was seen on all probes on the vehicle. At about 90 kft (421 sec) the modulation amplitude decreased with the angle of attack. At 80 kft (421 sec) the electron density began to decrease. The vehicle velocity was dropping below 10 kft/sec at that point, and both theoretical calculations and experience confirm that plasma effects are negligible for velocities below this value.

#### 6.4.2 PROBES ES-1 AND ES-2 ( $S/R_N \approx 2.40$ )

Probe ES-1 was positive-biased and probe ES-2 was negative-biased, and both were stepped sequentially from 15V to 30V and back. The complete data for  $\pm 15V$  is shown in Figure 34(a) and that for  $\pm 30V$  in Figure 34(b).

Both probes displayed anomalous behavior when biased at 15V. Examination of Figure 34(a) shows that at  $\pm 15V$ , both ES-1 and ES-2 remain fixed at the lower level of their sensitivity for part of a spin cycle. For ES-2 the response appears to be normal after 413 sec; for ES-1 the response becomes normal after 415 sec.

The third flight had been the first to include a variable-bias probe as part of the reentry vehicle instrumentation. The probe was negative-biased and was stepped at -5, -15, and -30 V. The data for -15 V and -30 V was normal, but the -5 V data exhibited the same trend as that of the  $\pm 15$  V probes on the fifth flight. The -5 V data was completely missing down to approximately 220 kft. At that point the current rose abruptly to a level that was normal for that altitude. The response stayed normal for the rest of the flight.

In analyzing the events of the third flight, it was thought that the drop from the -30 V level to -5 V had created a capacitance problem in the probe circuit, preventing the flow of probe current when the current was below some initial level. The probe circuitry was modified for the fourth flight but this did not solve the problem: data was not obtained at the  $\pm 5$  V levels until the reentry vehicle had reached an altitude of 170 kft. Current blockage was evidently not responsible.

For the fifth flight it was decided to dispense with the 5 V bias level and avoid its attendant anomaly. The subsequent reappearance of the problem in the 15 V data cannot be explained at this time. An additional aspect of the 15 V data is that it appears to be completely normal on the windward side. This can be seen by comparing the peaks of the ion density obtained at  $\pm 15$  V from ES-1 and ES-2 with the  $\pm 15$  V data obtained from the pair of probes ES-4 and ES-5 at  $S/R_N = 1.77$ . Considering the difference in location, the probes are in good agreement. In other respects, the ES-1 and ES-2 operating at  $\pm 15$  V produced data similar to that from ES-4 and ES-5 already discussed. The electron density is seen to be always around 200 times less than the corresponding positive-ion density during the period of normal probe response ( $t > 415$  sec). For ES-1, the windward and leeward electron densities differed by a factor of 4. For ES-2, the positive-ion densities differed by a factor of 5.

When the probes are biased at  $\pm 30V$  [Figure 34(b)] their responses are seen to be normal, except that the windward-leeward modulation is missing for ES-2 (positive ions) during the plasma buildup time from 410.3 to 411.2 sec (260 to 240 kft). This is similar to the behavior of probe ES-4 in the corresponding time

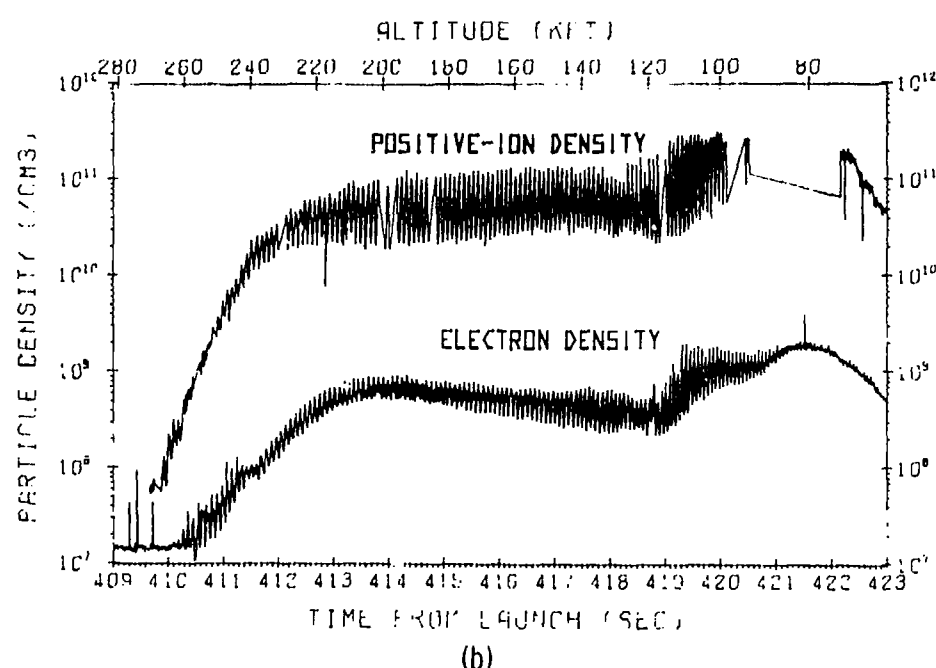
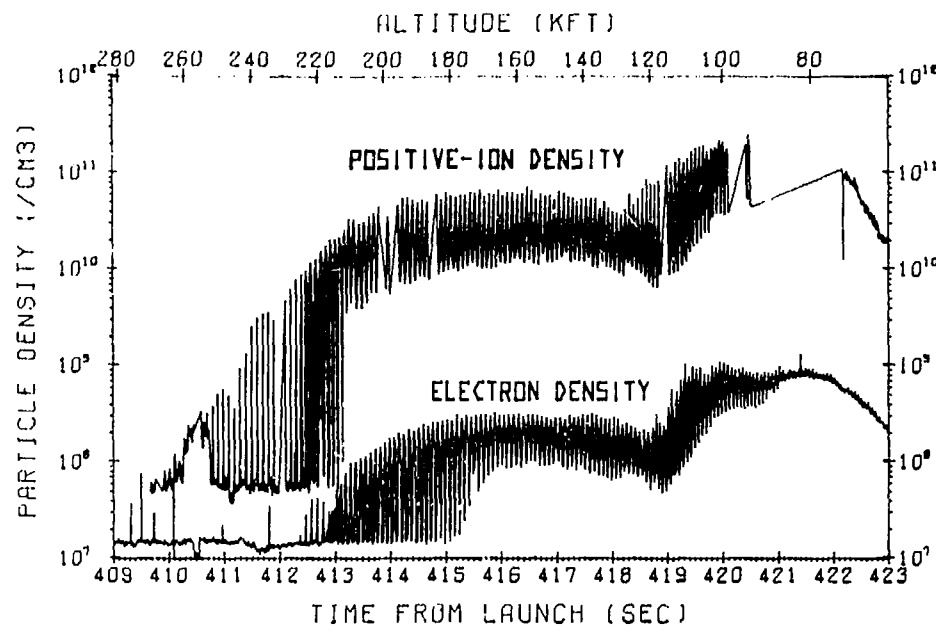


Figure 34. Charged-Particle Densities Measured at  $S/R_N = 2.40$  on Fifth Flight [probes ES-1 and ES-2 (a) biased  $\pm 15V$ ; (b) biased  $\pm 30V$ ]

period. Here, too, the electron density is seen to be always about 200 times less than the positive-ion density. A change in the modulation character of the electron density curve is apparent between 414 and 416 sec. This is the same time span over which the reflection coefficient of the low power test antenna was higher on the leeward side than on the windward.

With the exception of the missing high-altitude data when they were biased at  $\pm 15$  V, these probes provided data throughout reentry, showing the onset of turbulence, the decrease in angle of attack, and disappearance of plasma effects at altitudes below 80 kft. These aspects will be discussed when all the probe data is summarized to identify systematic changes in the ionized flow over the vehicle and its interaction with the Teflon ablation products.

#### 6.4.3 PROBES ES-7 and ES-8 ( $S/R_N = 4.44$ )

The data from probe ES-7 (+15 V) and ES-8 (-15 V) is plotted in Figure 35. Probe ES-8 shows a longer buildup time (410 to 413 sec) than that measured by the probes located forward on the vehicle. As was true for the other negative probes, however, the normal windward-leeward modulation is missing during this time. Eventually (417 sec), the positive-ion density reaches a value equal to

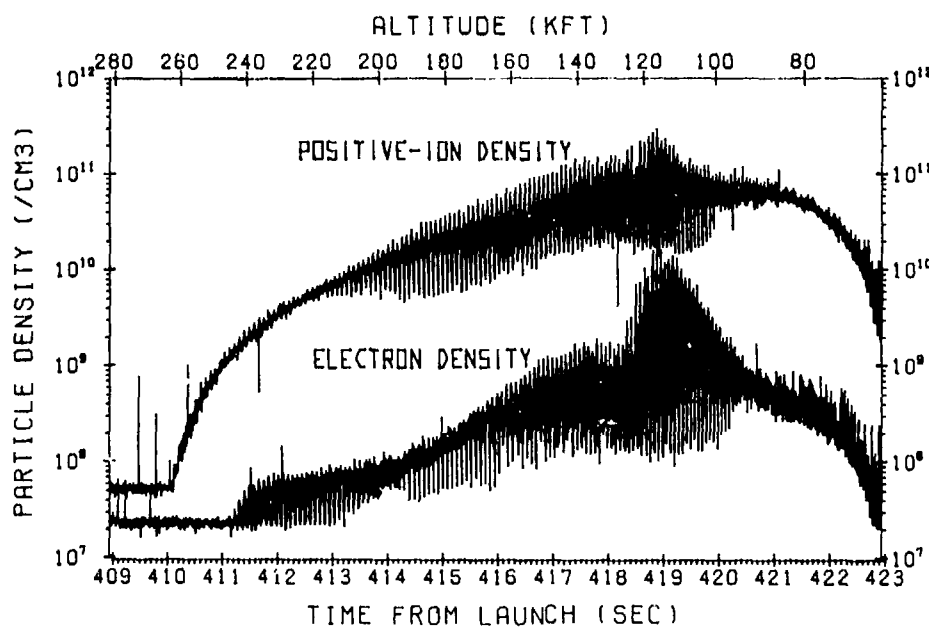


Figure 35. Charged-Particle Densities Measured at  $S/R_N \approx 4.44$  on Fifth Flight (probe ES-7 biased +15V; ES-8 biased -15V)

the value measured at the forward probes. This effect is contrary to the anticipated result—that the ion density would decrease owing to a natural relaxation, as in the absence of additive.

The data from probe ES-7 is most interesting. At 200 kft the modulation of the probe response changes character. This is about the same altitude at which the reflection coefficient (measured by the TM test antenna) began to show a higher value between the windward and leeward positions than at either of those positions. Above 200 kft (414 sec), the electron densities as measured by this probe are lower than the densities measured by the probes at the forward positions; for example, above 200 kft, the electron density is lower by a factor of 4 on the windward side. These are normal findings. Below 200 kft, however, the opposite is true: the electron densities at the rear of the vehicle are greater than at the forward positions. At 160 kft for example, the electron density is greater by a factor of 4 at  $S/R_N = 4.44$ . A somewhat similar result was seen on the liquid-injection flight but throughout that test the electron density at  $S/R_N = 4.44$  was greater than that measured by probes directly behind the shoulder injection ports.

#### 6.4.4 PROBES ES-3 and ES-6 ( $S/R_N = 2.40$ )

As previously mentioned (Sec. 6.3), probes ES-3 and ES-6, both biased positive (+15 V), were used in conjunction with probe ES-1 for the purpose of detecting any nonuniform ablation. Both were located at the same body station ( $S/R_N = 2.40$ ) as the probe pair ES-1 and ES-2, but ES-3 was placed about  $120^\circ$  clockwise and ES-6 about  $120^\circ$  counterclockwise around the vehicle from them. The electron density-versus-altitude calculated from the ES-3 data is shown in Figure 36(a); that from the ES-6 data is shown in Figure 36(b). To within the probe accuracy (factor of 2), there are no significant differences between the two.

There is some disagreement between the data from ES-1 and that from ES-3 and ES-6. Although all three probes became sensitive to the plasma at the same time and remained in agreement upon reaching the same laminar peak density, the rise in electron density measured by ES-3 and ES-6 was nevertheless more gradual than that measured by ES-1.

It is doubtful whether the behavior of ES-3 and ES-6 can be attributed to non-uniform ablation since the probability is slight that nonuniform ablation would cause similar effects at two probes located  $120^\circ$  apart. There is still the possibility that ES-1 was seeing a nonuniform effect. But the data from probe ES-4 (at  $S/R_N = 2.09$ )—which was closer to ES-3 and ES-6 than to ES-1—agrees with the data measured by ES-1, which would negate this possibility.

We have no definite explanation for these variances. Since probes ES-3 and ES-6 were on the same commutator and shared common circuit elements, it may be that a malfunction of these elements caused the observed behavior.

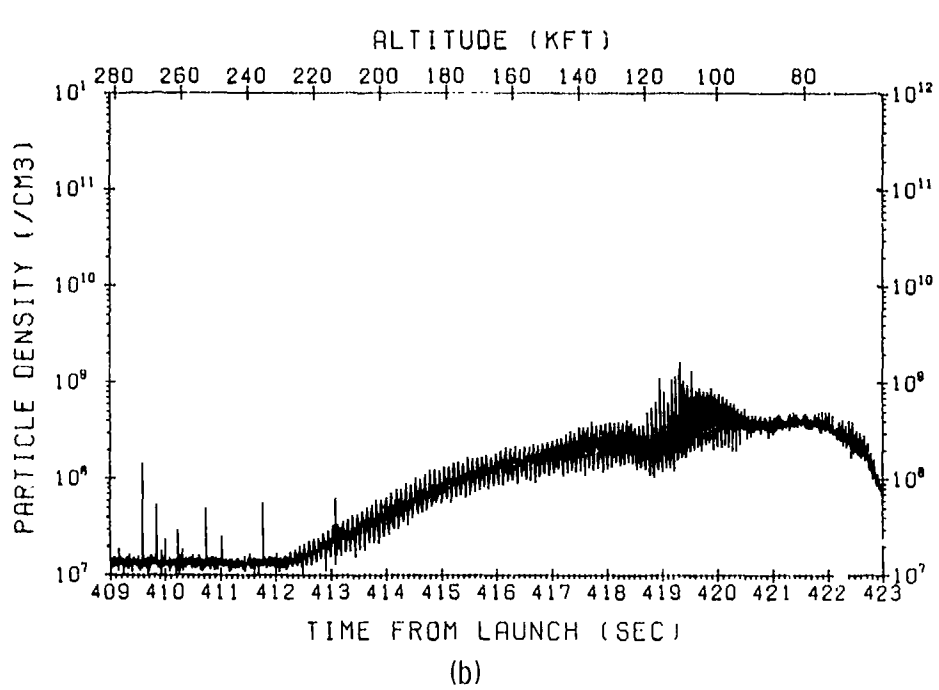
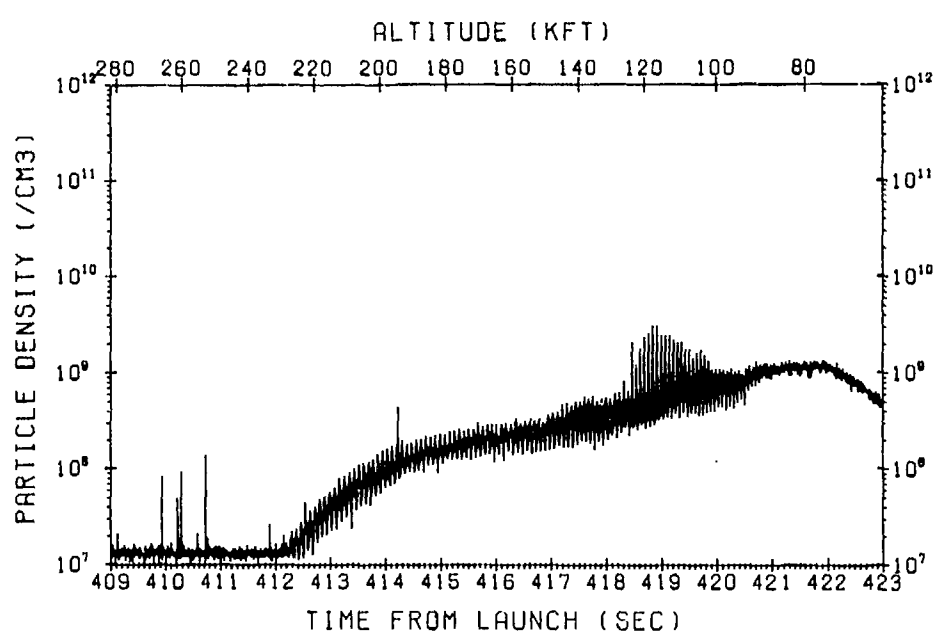


Figure 36. Electron Density Measured at  $S/R_N \approx 2.40$  on Fifth Flight [(a) ES-3, (b) ES-6]

#### 6.4.5 DETERMINATION OF SIGNIFICANT REENTRY EVENTS FROM PROBE DATA

Table 6 lists significant events for each probe, with the time and altitude at which they occurred. The time of the onset of plasma effects (column 1) is included only for the sake of completeness. This onset is not a flow event but a function of the lower level of sensitivity of each probe.

Except for probes ES-3 and ES-6 (see Sec. 6.4.4), all the probes forward on the reentry vehicle indicated peak charged-particle density at roughly the same time and altitude (column 2).

Column 3 lists the time at which the probe response, having reached a plateau, once again begins to increase; column 4 gives the time it ceases. The increase in measured density, attributed to the onset of boundary-layer turbulence, is seen to begin at the rear of the vehicle and progress forward. This trend becomes most apparent on averaging the times at which the increase begins and ends for all the probes located at one station on the vehicle. These average times, along with the corresponding altitudes, are shown in the inserts in columns 3 and 4. The altitudes are plotted in Figure 37 as a function of body station. For ease of comparison the theoretical curve (Figure 6) is replotted here. It is seen that the flight data bounds the predicted values for body stations  $S/R_N = 4.44$  and  $S/R_N = 2.40$ . The onset of turbulence occurs at a higher altitude, and full turbulence is reached at a lower altitude, than predicted. Considering the uncertainties involved, the agreement between the observed and the predicted onset of turbulence is quite good. The predicted probe response is not, however, borne out by the flight data for  $S/R_N = 1.77$ . This station is closest to the Teflon heat shield. The effect of the mass addition from the ablation process may have been to retard the onset of boundary-layer turbulence in this region.

It should be pointed out that the increase in electron density measured at probe ES-7 is greater than that at the forward probes. Also, below 100 kft, when the charged-particle densities measured by ES-7 and ES-8 start to fall, the amplitude of the fluctuations is greater than that measured at the forward probes. These results are consistent with the fact that transition begins at the rear and moves forward, and the turbulent fluctuations at the rear have therefore had a longer time to intensify.

The last two columns of Table 6 give the altitudes and times at which the windward-leeward modulation of the probe data ceases and the particle density begins to fall off. The modulation ceases because the angle of attack of the vehicle decreases to zero owing to atmospheric drag; the falloff in particle density is due to the slowing down of the vehicle to below a critical velocity. Each effect should be observed at the same time for all probes. Examination of the data shows this to be roughly the case.

Table 6. Significant Reentry Events Determined From Probe Data

Event * Probe	Onset of Probe Response	Peak Density Reached	Onset of Transition to Turbulence	End of Transition to Turbulence	Avg	End of Windward- Leeward Modulation	Beginning of Fall-off in Density
ES-5 Pos. Ions S/RN = 1.77; $\phi = 184.5^\circ - 15 V$	409.6 (270)	413.4 (208)	419.1 (113)	419.2 (100)	420.0 (100)	420.1	
ES-4 Electrons S/RN = 1.77; $\phi = 175.5^\circ + 15 V$	411.4 (240)	413.3 (209)	419.3 (110)	420.2 (97)	420.2 (98)	421.0 (88)	421.7 (79)
ES-2 Pos. Ions S/RN = 2.40; $\phi = 4.5^\circ - 15 V$	409.7 (269)	413.3 (209)	418.2 (128)	419.6 (105)	419.6 (105)		
ES-1 Electrons S/RN = 2.40; $\phi = 355.5^\circ + 15 V$	412.4 (224)	413.6 (204)	418.7 (120)	419.3 (110)	419.3 (110)	421.0 (88)	421.5 (93)
ES-2 Pos. Ions S/R = 2.40; $\phi = 4.5^\circ - 30 V$	409.7 (269)	413.5 (206)	418.3 (126)	418.5 (113)	419.1 (113)		
ES-1 Electrons S/RN = 2.40; $\phi = 355.5^\circ + 30 V$	410.2 (261)	413.5 (206)	418.9 (117)	419.3 (110)	419.4 (111)	421.0 (88)	421.6 (90)
ES-6 Electrons S/RN = 2.40; $\phi = 249^\circ + 15 V$	412.1 (229)	414.1 (196)	418.2 (128)	418.8 (118)	418.8 (118)	420.5 (93)	421.9 (78)
ES-3 Electrons S/RN = 2.40; $\phi = 111^\circ + 15 V$	412.2 (227)	415.3 (177)	418.6 (122)	419.3 (110)	419.3 (110)	420.5 (93)	421.8 (79)
ES-8 Pos. Ions S/RN = 4.44; $\phi = 4.5^\circ - 15 V$	410.1 (263)	412.4 (224)	418.3 (126)	419.3 (117)	418.9 (117)	421.1 (87)	421.1 (87)
ES-7 Electrons S/RN = 4.44; $\phi = 355.5^\circ + 15 V$	411.2 (244)	416.8 (151)	418.3 (126)	418.9 (117)	420.7 (90)	420.7 (91)	

\* Upper number in each block = Time from launch (sec); lower number = Altitude (kft)

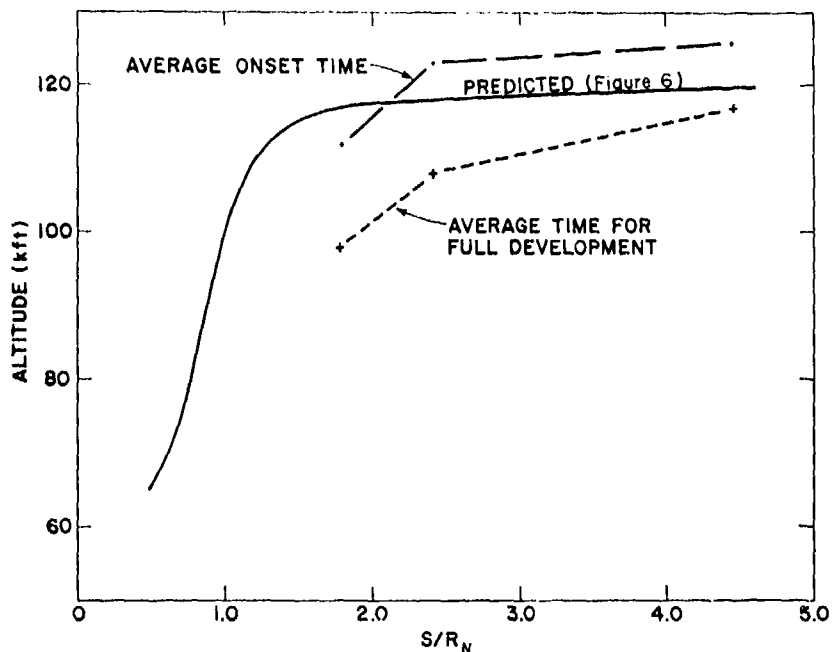


Figure 37. Comparison of Predicted and Measured Transition to Turbulence

## 7. COMPARISON OF THE ABLATIVE AND LIQUID-INJECTION FLIGHTS

### 7.1 Additive Comparisons

The rationale for establishing the amount of Teflon in the flow has been presented (Sec. 4.3). For the chemical-injection flight, a similar procedure was followed for each of the liquid Freon 114B2 pulses.<sup>18</sup> A comparison of the two sets of relative concentrations as determined by that approach is shown in Figure 38. The general trend of the curves is similar, with the value of the Teflon being consistently less than that of either of the corresponding Freon pulses. The method of calculating these relative concentrations is approximate, and some qualifying remarks are required.

The Freon mass should be compared with the air flow through the cross-sectional area determined by the penetration height of the individual liquid pulses. The vaporized Teflon would generally be confined to the boundary layer and so the mole fraction of the ablation products should be based on that flow. In the approximation used, both additives were compared with the mass flow in the entropy

18. Hayes, Dallas T., Herskovitz, Sheldon B., Lennon, John F., and Poirier, J. Leon (1974) Electrostatic probe measurements of chemical injection effects during a reentry flight test, J. Spacecraft and Rockets 11:388-394.

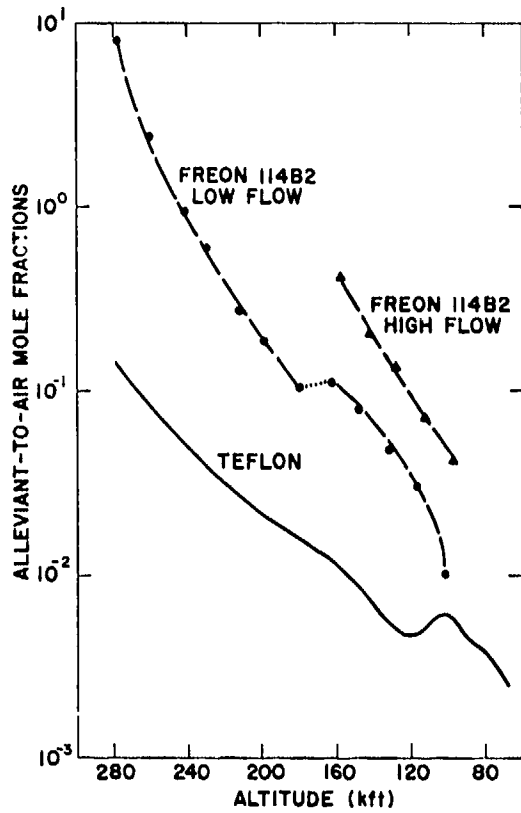


Figure 38. Relative Alleviant Concentrations

layer, which contains the high-temperature air from the nose. This approximation is not strictly valid for all altitudes. At the higher altitudes, both the liquid penetration and the boundary-layer effects extend over a considerable part of the shock layer. In this case the approximation is reasonable, and the comparisons should be essentially correct. At altitudes between 180 and 120 kft, the boundary layer containing the ablated Teflon remains laminar. In this low-altitude regime the boundary layer is not as large as the entropy layer, and the calculated Teflon mole fractions are therefore inaccurate. The penetration of the Freon pulses, however, continues to be on the order of the thickness of the entropy layer, so those ratios remain consistent.

A final summary of these considerations as they apply to the results shown in Figure 38 is required. Both alleviant concentrations in the high-altitude regime proved to be reasonable estimates. At the lower altitudes, the liquid Freon levels would still be valid. The Teflon levels, however, should be compared with a smaller air flow than was used; below 180 kft they represent an underestimation

of the actual ratios. The adjusted values should be closer to the equivalent liquid levels. These factors should be taken into consideration in any final evaluation of the results of the two experiments.

### 7.2 Probe Results

To compare the results of the Teflon and Freon 114B2 flights, we examine the data from a comparable pair of probes on each flight. Both pairs were flown at the same position ( $S/R_N = 2.40$ ), and both pairs were biased the same (one of each biased +30 V; the other, -30 V). Figure 39 presents the case for Freon; Figure 34(b) is the comparable case for Teflon.

The marked difference between the Freon and Teflon data is due to the difference in the additive techniques. In the case of Teflon, the alleviant enters the flow field continuously. As previously mentioned (Sec. 6.4.2), the effect of the ablation products is to lower the electron density but there is no apparent cooling of the flow. There is an absence of windward-leeward modulation during the ion-density buildup period but the density during this time span is roughly the same as would be measured on the windward side in the absence of the ablation products.

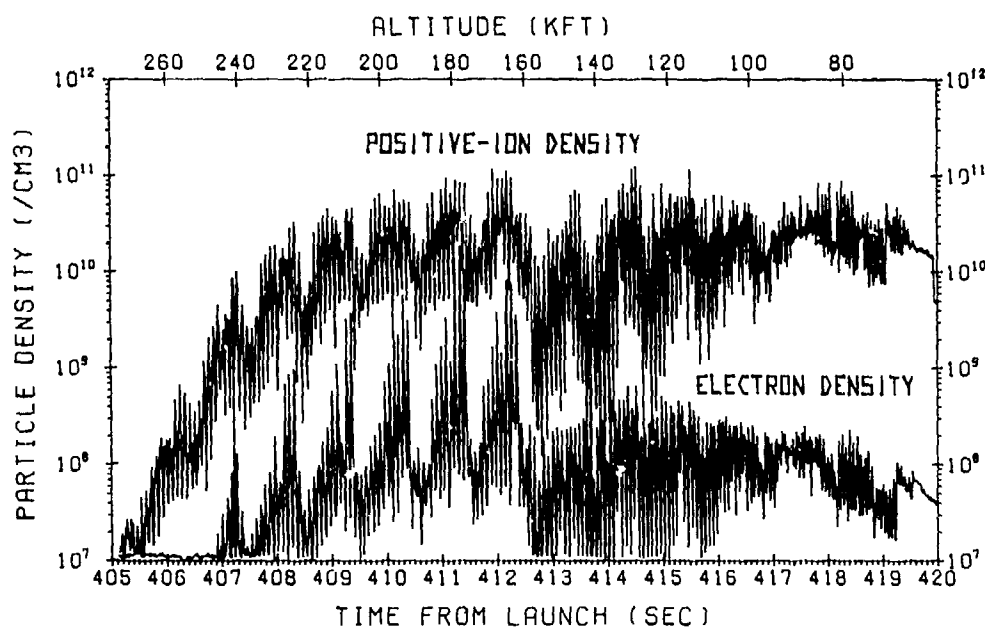


Figure 39. Typical Charged-Particle Concentrations Measured During Fourth Flight (Freon-injection: pair of electrostatic probes at  $S/R_N = 2.40$ , biased  $\pm 30V$ )

Examination of Figure 39 shows a much different picture for Freon. Superposed on the rapid windward-leeward modulation is a slower modulation of the probe response, caused by the pulsed nature of the liquid injection. Cooling of the flow is apparent in that during each pulse the ion density is lowered. During the interpulse period the ion density returns to the value that is normal when no additive is present; the electron density does not show a similar recovery. After 412 sec (~160 kft) the figure reflects actuation of the high-flow pulses in the further suppression of the electron density, to a value below  $10^8 \text{ el/cm}^3$ . The cooling effect on the ions, which is apparent only during the pulse period, becomes less pronounced as the altitude decreases.

The increase in ion and electron densities shown by all probes at about 120 kft in the Teflon-ablation flight has been attributed to the transition to a turbulent boundary layer. In the liquid-Freon injection flight, an increase of this nature was shown only by the probe at  $S/R_N = 1.77$  (Figure 32), which was unaffected by the additive.

For all probes affected by the additive the result was similar to that shown in Figure 39, with no increase in either the electron or ion density in this altitude regime. The mass addition from the surface in the nose region did not represent a significant perturbation of the normally developed flow. The liquid additive, however, having been injected with a strong dynamic pressure component, may have strongly perturbed the existing flow and introduced considerable cooling. This could have suppressed the changes in electron density associated with an unperturbed transition to turbulent flow.

The reentry velocity in both flights dropped below 10 kft/sec at about 80 kft, after which the charged-particle density began to decay, as anticipated. In the ablative flight, the windward-leeward modulation had ceased before the vehicle reached this altitude. In the liquid-additive flight, the modulation persisted below 80 kft.

Figure 40 presents the minimum value of the windward electron density measured during each pulse on the liquid-injection flight. The corresponding values for the ablation flight are also shown, along with values of the unperturbed electron density measured by a probe located at the same body station on the third Trailblazer flight test. It is seen that the measured decrease in electron density is greatest on the liquid-injection flight, being about three orders of magnitude less than that measured on the nonadditive flights. On the ablative flight the electron density is about 1/200th of the unperturbed value.

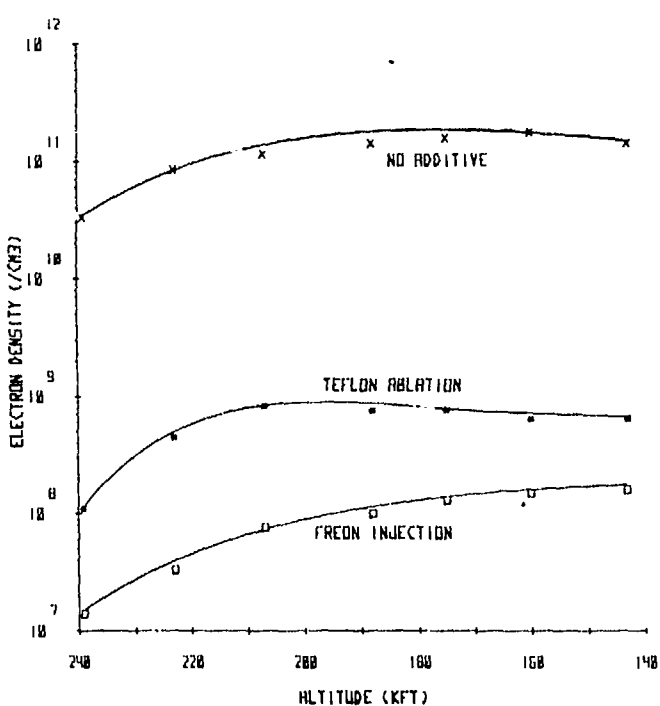


Figure 40. Effect of Alleviants on Electron Density

### 7.3 Antenna Results

Measurements of antenna performance during the last three flight tests can be compared in a number of ways. Only a few are considered in this preliminary report.

On all nonadditive flights, the power reflection coefficient at a given altitude was always greater on the windward side than on the leeward side. At plasma onset it typically displayed a sharp increase to about 0.9, and it remained at that value down to altitudes of 90 kft. (Below this altitude, aerodynamic heating caused melting of the nose cone or loss of radar tracking.)

In contrast, the reflection coefficient observed on the Freon-injection flight did not exceed 0.3 on the windward axis and 0.8 on the leeward axis. Not only did the leeward value exceed the windward value on this flight, but the maximum values were attained at a lower altitude.

On the Teflon-ablation flight, the windward and leeward power reflection coefficients each reached a value of about 0.6, but at different altitudes. The chemical additive tended to suppress the antenna mismatch on each axis; however, the variation in mismatch with spin is considerably more complex on the additive

flights. This indicates that the penetration and mixing of the additive is a sensitive function of angle of attack and body-axis position.

The maximum change in interantenna coupling observed on the Teflon flight was not greatly different from that seen on the Freon-additive flight but the responses differed in two respects. On the Teflon flight the antenna coupling showed no large variation with spin, as on the Freon flight. Then, for most of the Teflon flight the windward-leeward values varied less than a few decibels; on the Freon flight these values varied about 6 or 8 dB for the entire reentry trajectory. These results again demonstrate that the additive penetration, mixing, and subsequent quenching, were strongly dependent on the three-dimensional flow structure.

The reduction in total signal attenuation shown in Figure 41 graphically illustrates the improvement in performance caused by both chemical additives. Increases of up to 30 dB in received signal intensity were observed. It should again be emphasized that the additive concentrations in the two flights were different (Figure 38). Both Freon injection and Teflon ablation are effective methods for improving the performance of a microwave antenna system during reentry.

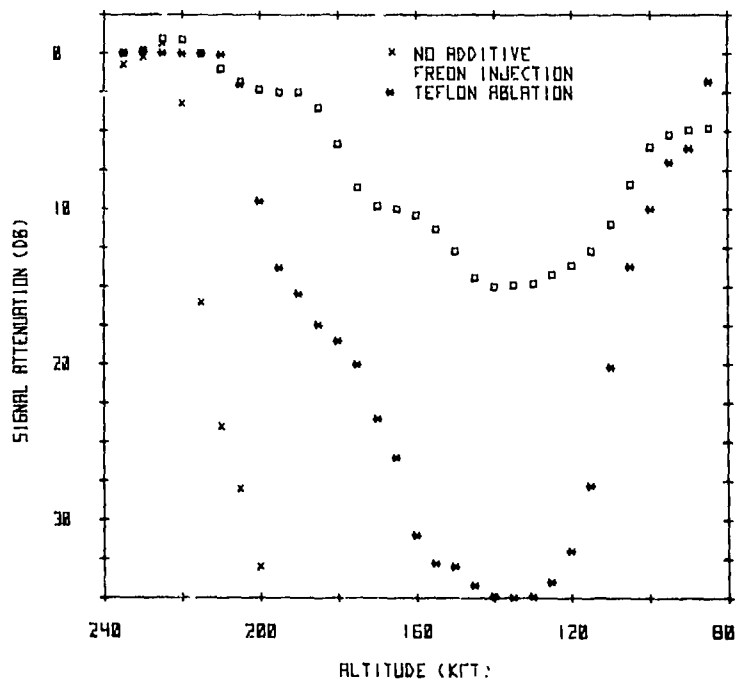


Figure 41. Effect of Alleviants on Total Signal Attenuation

## 8. DISCUSSION OF EXPERIMENTAL RESULTS

The fifth in the series of Trailblazer II flights was successfully carried out. The principal results are summarized as follows:

- 1) With the sole exception of the ablation gauges, all electrical, transmission, and electrostatic probe, devices functioned properly. The Teflon-ablation coating behaved according to expectations.
- 2) Both electron and positive-ion densities were measured in the presence of ablative products. The results definitely confirmed that electrophilic action was taking place. The measured electron density was always approximately 1/200th of the ion density.
- 3) Ion density values were essentially identical with those obtained in the non-additive flights, indicating that cooling was not a significant factor.
- 4) The probe configuration on this flight places dual constraints on theoretical predictions. Independent measurement of both electron and positive-ion densities means that any additive analysis will have to satisfy both values.
- 5) In addition to charged-particle density measurements at the antenna, the flight also provided information on the downstream history of the additive. (The pair of electrostatic probes at  $S/R_N = 4.44$  presented data on the charged species at this location.)
- 6) Spin and angle-of-attack effects were observed. The levels of additive-flow interaction were different, depending on whether the measurement was being made on the windward or leeward axes, or between these two positions.
- 7) On the nonadditive flights, no data had been obtained below 100 kft. On this fifth flight, useful probe data was obtained to 80 kft. Below this altitude, antenna signals returned to freespace levels.
- 8) The apparent transition of laminar to turbulent boundary-layer flow was observed.
- 9) The probe measurements of windward electron density at altitudes above 200 kft were lower at the rear ( $S/R_N = 4.44$ ) than at the shoulder of the vehicle. Below 200 kft, the density at the rear was higher than at the shoulder.
- 10) The Teflon additive reduced mismatch of the test antenna. It also greatly decreased total signal attenuation.
- 11) Comparison of electrostatic probe and microwave data indicated that below 200 kft, alleviation occurred principally near the surface of the vehicle.
- 12) The performance of the TM/TX antenna showed that alleviation continued to the rear of the nose cone.
- 13) On the bare-body flights, plasma effects on the probes and antennas had always been greater on the windward axis. This was not the case on the Teflon flight.

14) Preliminary comparison of the solid Teflon ablation and liquid-Freon injection results indicates that both are effective methods of reducing the free-electron concentration during reentry.

#### 9. CONCLUSIONS

This experiment proved that a Teflon coating can effectively reduce the electron density surrounding a reentry vehicle. Under the conditions of this fifth flight, the Teflon ablation acted as an electrophilic agent, with no significant cooling. The results varied, depending on altitude, orientation of the vehicle (whether windward or leeward), position on the vehicle (whether at the shoulder or the rear), and various other measurement conditions.

Although the antenna and probe results indicate that the Freon 114B2 used on the fourth flight had apparently achieved a higher degree of alleviation than the Teflon used on this fifth flight, it should be kept in mind that the concentrations, penetration, and mixing of the additives with the flow were not exactly the same. A more comprehensive analysis is required before we can make a definitive statement on the relative efficiency of the two techniques. We are now making additional comparisons between the data from both flights.

## References

1. Poirier, J. Leon, Rotman, Walter, Hayes, Dallas T., and Lennon, John F. (1969) Effects of the Reentry Plasma Sheath on Microwave Antenna Performance: Trailblazer II Rocket Results of 18 June 1967, AFCRL-69-0354.
2. Hayes, Dallas T., and Rotman, Walter (1973) Microwave and electrostatic probe measurements on a blunt reentry vehicle, AIAAJ 11:675-682.
3. Hayes, Dallas T., Herskovitz, Sheldon B., Lennon, John F., and Poirier, J. Leon (1972) Preliminary Report on the Trailblazer II Chemical Alleviation Flight of 28 July 1972, AFCRL-72-0640.
4. Strategic Reentry Technology Program (STREET A) (1970) Task 7.5: Nose Tip Ablation Phenomena, Final Rpt, Vol. II, SAMSO-TR-70-247.
5. van Driest, E. R., Blumer, C. B., and Wells, C. S. (1967) Boundary-layer transition on blunt bodies—effect of roughness, AIAAJ 5:1913-1915.
6. Nosetip Design Analysis and Test Program (NDAT) (1971) Final Rpt, Vol. I, Part 1, SAMSO-TR-71-11.
7. Detra, R. W., and Hidalgo, H. (1961) Generalized heat transfer formulas and graphs for nose cone reentry into atmosphere, ARSJ 31:318-321.
8. Martin, J. J. (1966) Atmospheric Reentry: An Introduction to its Science and Engineering, Prentice-Hall, p. 114.
9. DeBolt, H. E., and Port, W. (1963) Thermochemical Equilibrium Studies of Ablative Heat Shield Materials, (Task 3.2, REST Project), RAD-TM-63-27, Tech Memo for AFBSD by AVCO, 7 June 1963.
10. Lennon, John F. (1973) Trailblazer II Rocket Tests on the Reentry Plasma Sheath: Vehicle Performance and Plasma Prediction (Flights No. 1-3), AFCRL-TR-73-0317.
11. Pergament, H. S., and Kau, C. (1974) A Computer Code to Predict the Effects of Electrophilic Liquid Injection on Reentry Plasma Sheath Properties, AFCRL-TR-74-004, Contract No. F19628-93C-0045, Aerochem. Res. Lab., Inc.

## References

12. Hayes, Dallas T., and Lennon, John F. (1974) In preparation.
13. Skinner, G. B., and Ringrose, G. H. (1965) Shock-tube experiments on inhibition of the hydrogen-oxygen reaction, J. Chem. Phys. 43(No. 1):4129-4133.
14. Lennon, John F., and Poirier, J. Leon (1974) Interpretation of Microwave Antenna Results from a Reentry Flight Test: A Comparison of Methods, AFCRL-TR-74-0389.
15. Scharfman, W. E., and Bredfeldt, H. R. (1967) Experimental Studies of Electrostatic Probes for the Reentry Measurements Program, Phase B, Subcontract 611603 under Prime Contract 30-0690 AMC-333(Y), SRI Project 6138, Stanford Research Institute, Menlo Park, Calif.
16. Bohm, D., Burhop, E. H. S., and Massey, H. S. W. (1949) Use of probes for plasma exploration, Chap. 2 in The Characteristics of Electrical Discharges in Magnetic Fields, Guthrie, A., and Wakerling, R. K., Eds., McGraw-Hill.
17. Lew, H. G. (1974) Angle-of-Attack Effects on Electron Density Distribution Over Blunt Bodies, AFCRL-TR-74-0354, Contract No. F19628-72C-0070, General Electric (Doc. No. 74 SD 2113).
18. Hayes, Dallas T., Herskovitz, Sheldon B., Lennon, John F., and Poirier, J. Leon (1974) Electrostatic probe measurements of chemical injection effects during a reentry flight test, J. Spacecraft and Rockets 11:388-394.

## **Appendix A**

### **Ablation Gauges**

The Trailblazer II Teflon-ablation flight carried five breakwire ablation gauges at various locations in the Teflon-covered nosecap. The gauges were designed to produce a voltage that varied in correspondence with the recession of the ablation coating. The gauges failed to operate as expected. The output voltage remained constant, an indication that the breakwires did not fail. A possible explanation of this result is examined in Sec. A4.

#### **A1. BACKGROUND**

Ablation sensors can be divided into five categories: breakwire, variable capacitor, thermocouple, radioactive, and photocell. The breakwire gauge was used on this flight because of its inherent simplicity of construction and external circuitry.

The particular device we used was modified from an Avco Government Products Group design intended for an Air Force Weapons Laboratory hypersonic rocket sled test (TEMPESTA). It consisted of an array of fine aluminum wires (0.005 in. in diameter) set at varying depths in a Teflon plug. Five of these plugs were inserted from the inside through holes bored through the Teflon covering and substructure of the nose cone so that the external surface of each plug was flush with the ablation surface.

Laboratory simulation of reentry showed that the Teflon on the nose cone and the Teflon plug recede at the same rate. The aluminum breakwires are thus sequentially exposed to the hot gas flow, and they either melt or break. As each wire fails, the net resistance of a parallel-resistor network increases, producing a concomitant increase in the output voltage.

## A2. THE ELECTRICAL CIRCUIT

The breakwire-resistor network sketched in Figure A1 was fabricated on one end of the Teflon body of the ablation gauge. The leads from the gauge connect to a power supply through resistors  $R_1$  and  $R_2$ . These resistors divide the input voltage and limit the circuit current. With  $R_1 = 3.2\text{ k}\Omega$  and  $R_2 = 6.8\text{ k}\Omega$ , we get an approximate 3:1 voltage division;  $R_1$ , however is shunted by the ablation-gauge internal resistor network. With all breakwires intact, the impedance of  $R_2$  in series with the internal resistor network is  $211.4\Omega$ , thus producing a 16:1 voltage division with  $R_1$ . As the breakwires fail, the resistance shunting  $R_2$  increases, causing the output voltage to rise. If the voltage produced with all breakwires intact is denoted  $E$  (equal to 1/16 of the input voltage), then the voltage produced with the

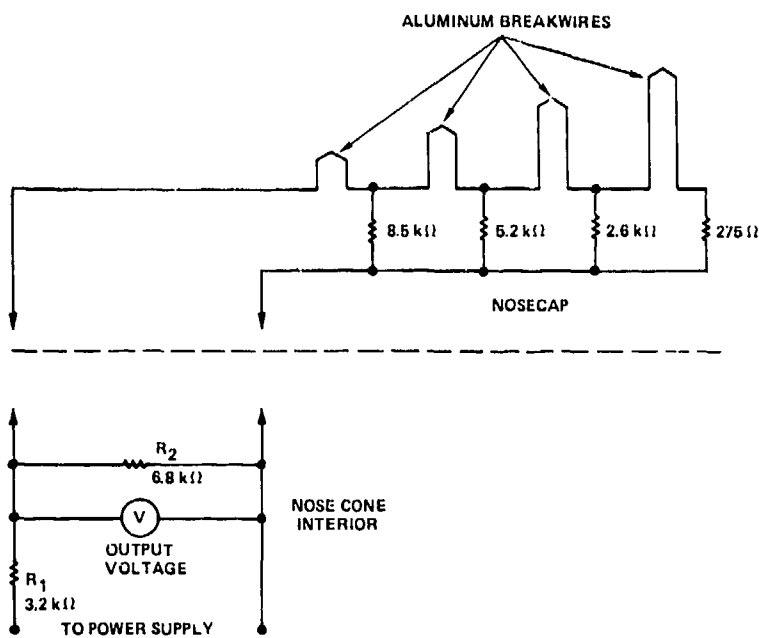


Figure A1. Electrical Subassembly of Ablation Gauge (schematic)

outermost breakwire gone is 4.35E; with two wires gone, it is 6.45E; three, 8.5E; and finally, with all breakwires gone, it is 12E (or 1/3.2 of the input voltage).

### A3. GAUGE CONSTRUCTION

In the AVCO gauge design, the resistor network was located external to the breakwires and thus required multiple leads. To simplify the circuitry, the resistor network was made an integral part of the ablation gauge. Subminiature chip resistors measuring 0.05 in. square by 0.013 in. thick were cemented to a Plexiglas sleeve bonded to the Teflon plug (Figure A2). Aluminum wire 0.005 in. in diameter was threaded through the Teflon plug and bonded to the outer edges of the appropriate resistors with conductive epoxy. Contact to the common side of the resistors (see Figure A1) was accomplished by means of a copper disk, also bonded to the resistors with conductive epoxy. The two leads to the external

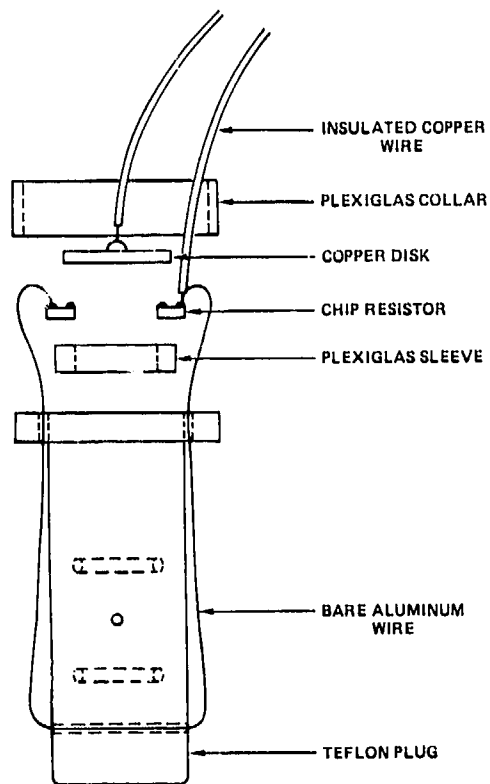


Figure A2. Assembly of Ablation Gauge  
(sketch)

circuit were attached, a Plexiglas collar cemented in place, and the entire sub-assembly potted. Figure A3 shows the assembled gauge and its constituent parts. The aluminum breakwires readily embedded themselves in the soft Teflon plug when the assembly was pressed into place on the nosecap.

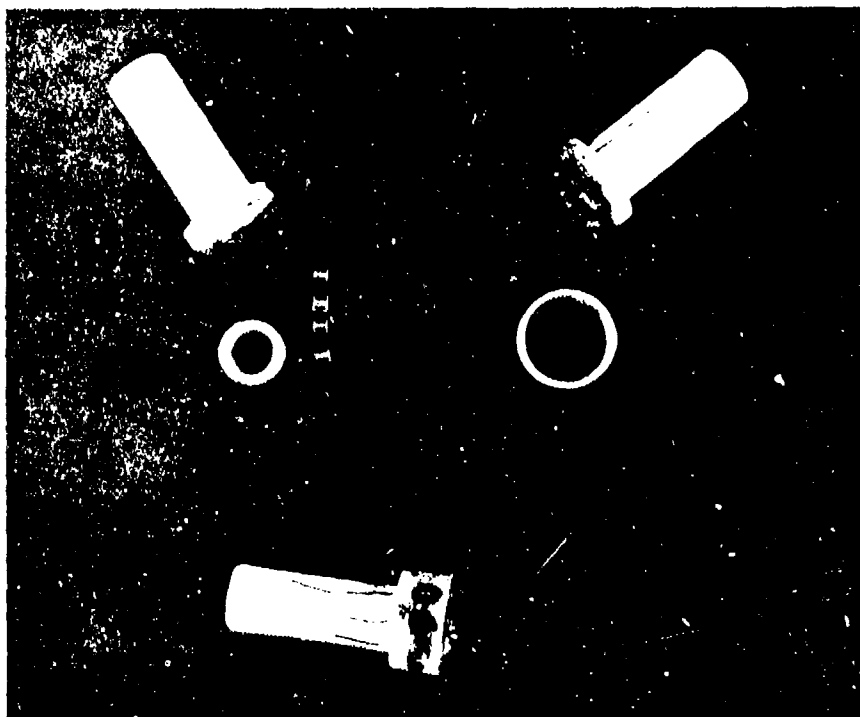


Figure A3. Ablation Gauge and its Constituent Parts ( $\sim 1\frac{1}{2} \times$ )

#### A4. RESULTS

The ablation gauges failed to operate. Other than a few spurious pulses, probably due to system noise, no stepped increase in monitor voltage was recorded on any gauge.

The breakwire concept had been proved in the laboratory. Tests of gauges embedded in 1-in.-diam. Teflon rods had shown that the aluminum gauge wires readily melted when subjected to heat sources such as a dc arc jet and an oxy-hydrogen torch, which respectively generated temperatures of approximately 4000°K and 2000°K.

We can postulate no definitive reason for the failure of these gauges to conform to expectations. Malfunction of the exceptionally reliable auxiliary electronic circuitry was unlikely. The gauge output voltage indicated four intact breakwires in each of the five ablation gauges. A short or open circuit would have produced a characteristic diagnostic output. The evidence is strong that the aluminum breakwires simply did not break. There is ample proof that the Teflon was indeed ablating. A nosecap temperature in excess of 933°K was required to melt the pure aluminum wires, and this was apparently not achieved. One hypothesis is that under the conditions encountered during reentry, the ablation process maintained a sublayer of relatively cool Teflon vapor adjacent to the nosecap surface.

## Symbols

A	probe area; capture area
E	electric field intensity
I	total current
$I_A$	axial moment of inertia
$I_T$	transverse moment of inertia
$P_g$	power received at ground station
$P_{inc}$	incident power
$P_{rec}$	received power
$P_{ref}$	reflected power
R	power reflection coefficient
$R_N$	nosecap radius
Re	Reynolds number
S	wetted length
T	temperature (°K)
V	velocity of vehicle; voltage
d	thickness of ablation layer
e	electron charge
$h_{cw}$	cold-wall enthalpy
$h_e$	enthalpy at outer edge of boundary layer
$h_{eff}^o$	effective heat of ablation (Btu/lb)
$h_{ST}$	stagnation enthalpy
$h_w$	hot-wall enthalpy
j	current density

## Symbols

$k$	Boltzmann's constant
$m$	particle mass
$n$	number density
$p$	pressure
$\dot{q}$	heat transfer rate
$t$	time from launch
$v$	thermal velocity of particle
$\Phi$	form factor for turbulent ablation
$\Psi$	form factor for laminar ablation
$\beta$	ballistic coefficient
$\gamma$	specific heat ratio; reentry path angle
$\epsilon_0$	permittivity of freespace
$\lambda$	probe sheath thickness
$\mu$	mobility
$\nu_{eN}$	electron-neutral particle collision frequency
$\nu_{-N}$	negative ion-neutral particle collision frequency
$\rho$	density
$\sigma_{eN}$	electron-neutral scattering cross section
$\sigma_{-N}$	negative ion-neutral scattering cross section
$\phi$	angular orientation of vehicle instrumentation measured clockwise from TX antenna

### Subscript Symbols

$\infty$	freestream condition
$e$	electron
$o$	original value
$SL$	sea level
$ST$	stagnation point
$+$	positive ion
$-$	negative ion